Ore Geology Reviews 91 (2017) 173–195

Contents lists available at ScienceDirect

Ore Geology Reviews

journal homepage: www.elsevier.com/locate/oregeorev

# Textures and U-W-Sn-Mo signatures in hematite from the Olympic Dam Cu-U-Au-Ag deposit, South Australia: Defining the archetype for IOCG deposits

Max R. Verdugo-Ihl[a,*], Cristiana L. Ciobanu[a], Nigel J. Cook[a], Kathy J. Ehrig[b], Liam Courtney-Davies[a], Sarah Gilbert[c]

[a] School of Chemical Engineering, The University of Adelaide, Adelaide, SA 5000, Australia
[b] BHP Olympic Dam, Adelaide, SA 5000, Australia
[c] Adelaide Microscopy, The University of Adelaide, Adelaide, SA 5000, Australia

ARTICLE INFO

*Keywords:*
Hematite
Trace elements
U-W-Sn-Mo compositional zoning
Olympic Dam
Iron-oxide copper gold deposits
Laser ablation inductively coupled plasma mass spectrometry

ABSTRACT

The textural characteristics and trace element geochemistry of hematite with U-W-Sn-Mo signatures from the Cu-U-Au-Ag orebody at Olympic Dam, South Australia, are documented. Olympic Dam is the archetype for iron-oxide copper–gold (IOCG) deposits where hematite is by far the most abundant mineral in the orebody. The deposit is located within hematite-bearing breccias (> 5% Fe) hosted by the ~1.6 Ga Roxby Downs Granite (RDG). Although such breccias are mostly derived from RDG, they also include volcanic clasts and sedimentary rocks. Samples cover the ~6 km strike length and ~2 km vertical extent of mineralisation, including hematite from the aforementioned lithologies. Hematite with U-W-Sn-Mo ('granitophile' elements) signatures is recognised throughout all lithologies and parts of the deposit. Hematite enriched in granitophile elements is represented by a variety of textures, of which zoned hematite, defined by oscillatory zonation patterns, is the most prominent and can be tied to the age of the RDG, and thus initiation of the IOCG system as confirmed by published U-Pb geochronology. Other categories of hematite with granitophile signatures include hematite resulting from replacement of pre-existing minerals (e.g., carbonates and feldspars), as well as replacement of previous oscillatory-zoned hematites. Matrix and vacuole filling hematite from volcanoclastic-dominated intervals also carry 'granitophile' signatures. In addition, some colloform types which likely post-date primary IOCG mineralisation are also rich in 'granitophile' elements. Trace element mapping and spot analysis by laser ablation inductively coupled plasma mass spectrometry (LA-ICP-MS) defines complex trace element signatures of hematite, which, in addition to the 'granitophile' elements, also comprise rare earth elements, high field strength elements, chalcogens and transition metals.

The distinct geochemical signature, characterised by enrichment in the 'granitophile' elements (up to wt% levels of U and W within individual zones, and up to thousands of ppm Mo and Sn) prevails throughout the hematite in the deposit irrespective of textures. Iron-oxides have been repeatedly formed, reworked and overprinted by subsequent cycles of brecciation, fluid-mineral reaction, remobilization, element redistribution and recrystallisation. Coupled dissolution-replacement reactions are discussed as having played a major role in the modification of textural and geochemical patterns in hematite, but also allow for widespread preservation of primary geochemical signatures. Despite its simple chemistry, the crystal-structural modularity of hematite can adapt and retain evolving fluid signatures. The reported trace element signatures are fully concordant with conceptual frameworks for the genesis of IOCG systems, and may be an inherent, albeit hitherto under-reported characteristic of other IOCG systems. Hematite is probably by far the most important W-, Sn- and Mo-bearing phase in the deposit by mass.

## 1. Introduction

An inherent feature of all iron-oxide copper gold (IOCG) deposits is the abundance of Fe-oxides, as either hematite (α-$Fe_2O_3$) and/or magnetite ($Fe_3O_4$), generally making the Fe-oxides by far the most dominant minerals (Hitzman et al., 1992). Iron-oxides are valuable sources of petrogenetic information, as they commonly contain trace elements at measurable concentrations, with patterns and variations among these trace elements that reflect evolving physiochemical conditions.

* Corresponding author.
*E-mail address:* max.verdugoihl@adelaide.edu.au (M.R. Verdugo-Ihl).

http://dx.doi.org/10.1016/j.oregeorev.2017.10.007
Received 11 August 2017; Received in revised form 8 October 2017; Accepted 10 October 2017
Available online 12 October 2017
0169-1368/ 

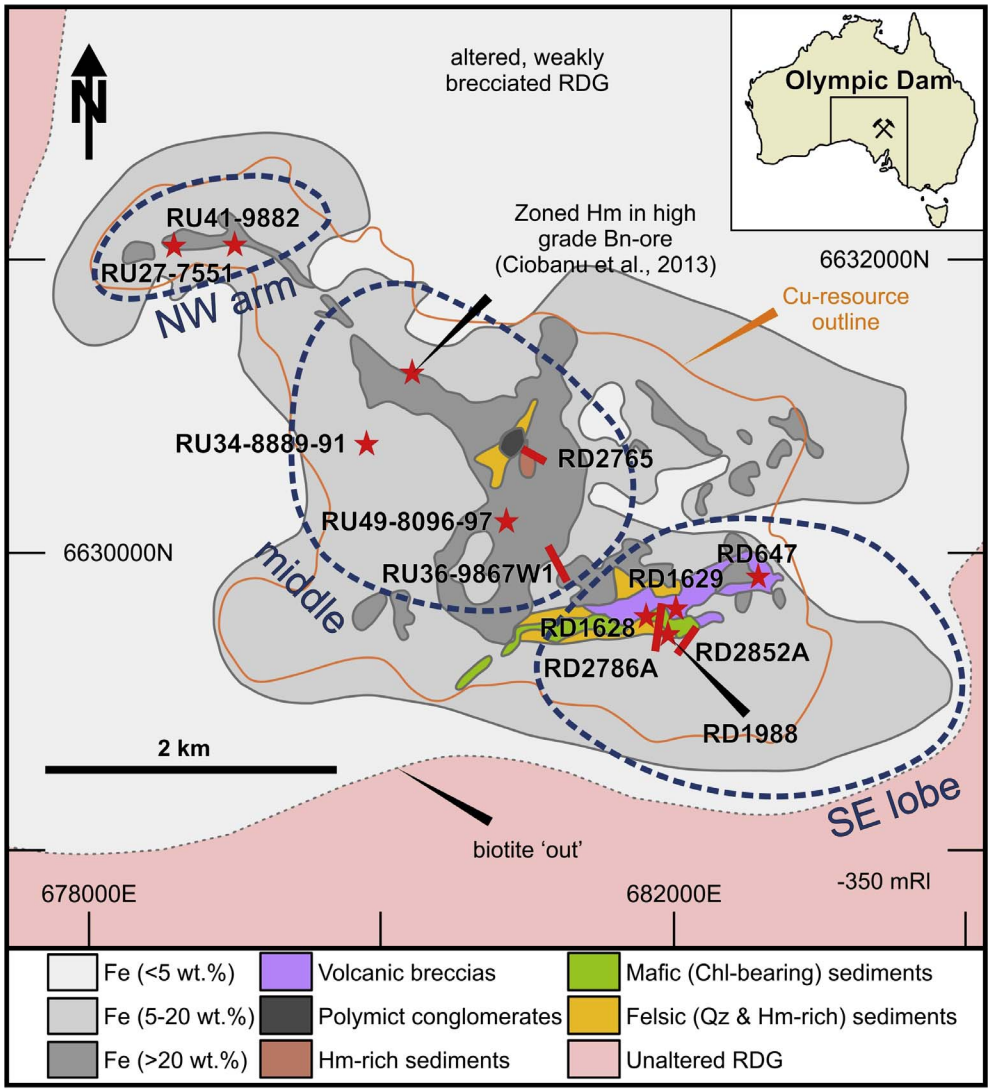


**Fig. 1.** Simplified geological sketch outlining the Olympic Dam Breccia Complex after Ehrig et al. (2012), indicating locations of sampled drillholes (stars: vertical drillhole; rectangles: oriented drillholes) and the distribution of main lithological units. The simplified map is projected at the −350 m RL mine grid below surface.

Recent literature is largely focused on trace element studies of mineral signatures by laser-ablation inductively-coupled plasma mass spectrometry (LA-ICP-MS; Cook et al., 2016 and references therein). Trace element signatures of magnetite from end-member IOCG deposits *sensu lato*, such as Kiruna (Sweden) and El Laco (Chile), have been obtained to constrain the debate on their magmatic versus hydrothermal origins (e.g., Dare et al., 2015; Knipping et al., 2015a,b; Broughm et al., 2017). Except for preliminary studies of hematite from Olympic Dam (OD) and satellite deposits such as Island Dam (e.g., Ciobanu et al., 2013, 2015; Cook et al., 2016; Keyser et al., 2017; Verdugo-Ihl et al., 2017), trace element geochemistry of Fe-oxides from IOCG-systems *sensu stricto*, and specifically hematite have not been studied in any great detail, despite being the main products of hydrothermal alteration, and therefore closely associated with the mineralising processes itself. The aforementioned studies have shown that hematite can incorporate a wide range of trace elements, including high field strength elements (HFSE), rare earth elements (REE) and Y (hereafter REY) and that these compositions vary with textures, location in the deposit and interconversion with magnetite. But more notable, oscillatory-zoned hematite from OD stands out by its enrichment in U (and radiogenic Pb), W, Sn, and Mo (hereafter 'granitophile' elements) (Ciobanu et al., 2013, 2015; Cook et al., 2016; Verdugo-Ihl et al., 2017). The incorporation of U and its decay products within the lattice of zoned hematite facilitates its use as a mineral geochronometer for directly dating hydrothermal ore-forming processes in IOCG deposits (Ciobanu et al., 2013; Courtney-Davies et al., 2016, 2017)

In this contribution, we document textural characteristics and trace element geochemistry of hematite from the Cu-U-Au-Ag orebody at OD (Ehrig et al., 2012), South Australia, the largest known IOCG system on Earth and considered the archetype of the IOCG deposit class (Hitzman et al., 1992). We address the petrography and trace element geochemistry of OD hematite, with emphasis on distinctive types enriched in U, W, Mo and Sn, which often display spectacular grain-scale compositional zonation. Other sub-types of hematite with granitophile-rich signatures are also documented as they can help track the sequence of incorporation and remobilisation of such elements during deposit evolution. The combination of textural and trace element data offers insights into the processes responsible for the genesis and overprinting of IOCG-deposits, as well as providing a temporal context for regional metallogenic events.

## 2. Geological background

Olympic Dam is a Cu-U-Au-Ag deposit (10,400 Mt @ 0.77% Cu, 250 ppm $U_3O_8$, 1 ppm Ag and 0.32 ppm Au; BHP Billiton, 2016) located in the central-northern part of the Olympic Cu-Au Province, South Australia. The Olympic Cu-Au Province is a N-S-trending metallogenic belt that extends ca. 700 km along the eastern margin of the Archean to Mesoproterozoic Gawler Craton. IOCG-style mineralisation in the province is spatially- and temporally-associated with a magmatic event at

~1.6–1.58 Ga that derived in the formation of a silicic large igneous province, encompassing the Hiltaba Suite (HS) and co-magmatic, bimodal Gawler Range Volcanics (GRV) (Fanning et al., 1988). These magmatic rocks intruded and unconformably overlie basement units, which in the OD district correspond to metasedimentary rocks of the Hutchison Group, deformed granitoids of the Donington Suite (ca. 1.85–1.81 Ga), and Wallaroo Group equivalents (ca. 1.76–1.74 Ga).

The deposit is hosted within the Olympic Dam Breccia Complex (ODBC; Reeve et al., 1990), which is confined to the Roxby Downs Granite (RDG; Fig. 1), an altered HS granitoid considered to form at a depth of 6–8 km (Creaser, 1989; Kontonikas-Charos et al., 2017a). Proximal to the deposit, the RDG displays a gradational continuum from altered, through fractured to brecciated lithologies, associated with an increase in the degree of Fe-metasomatism and multiple episodes of brecciation and replacement. The deposit formed beneath, and partly within, an active sedimentary basin, as indicated by locally well-preserved fragments of subaqueous sedimented facies incorporated within the breccias (McPhie et al., 2011, 2016). At least two generations of predominantly mafic-ultramafic dykes occur in the deposit: an early generation of GRV-associated dykes, roughly synchronous with IOCG mineralisation (Huang et al., 2016); and superimposed dolerites affiliated to ~820 Ma Gairdner Dyke swarms (Huang et al., 2015). At the deposit scale, OD is mineralogically zoned, featuring a roughly concentric vertical and lateral zonation with respect to Cu(-Fe)-sulphides from an outer/deeper pyrite-chalcopyrite (Py-Cp) zone through chalcopyrite-bornite (Cp-Bn) to a bornite-chalcocite (Bn-Cc) zone enclosing the largely sulphide-barren inner core (Ehrig et al., 2012). Such a pattern is considered to represent a primary feature of hypogene ore precipitation (Ciobanu et al., 2017). Additionally, a polymetallic signature is recognised at deposit margins (galena, sphalerite, and fahlores in the SE lobe). Unlike the sulphides, the distribution of U-minerals (uraninite, coffinite and brannerite) does not appear to follow a systematic deposit-scale zonation, although the proportion of uraninite tends to increase with Fe content (Ehrig et al., 2012).

Within the orebody, hematite is the main Fe-oxide, irrespective of sulphide zone, although magnetite can be locally dominant at depth and at deposit margins (Ehrig et al., 2012; Ciobanu et al., 2015). Copper grade broadly correlates with the intensity of Fe-metasomatism, meaning that the resource outline coincides with Fe-rich domains (Fig. 1).

High-precision U-Pb dating of magmatic and hydrothermal zircon in the RDG and ODBC shows that the earliest stages of brecciation and hydrothermal alteration are coeval with RDG crystallisation at ~1594 Ma (e.g., Jagodzinski, 2005). This temporal constraint is supported by U-Pb geochronological data for oscillatory-zoned hematite from two locations in the deposit, which overlap with the zircon ages (Ciobanu et al., 2013; Courtney-Davies et al., 2016).

## 3. Sampling approach

The present study was carried-out on a sample suite (58 hand specimens derived from 17 drillholes) representative of hematite in the ODBC throughout the ~6 km strike length through the SE lobe, the middle, and the NW arm and ~2 km depth of the deposit in the SE lobe (Table 1; Figs. 1 and 2; Electronic Appendix Fig. A1). The sampled lithologies include: (i) granite-rich breccias, generally clast-supported, containing fine-grained hematite as a matrix component and variably-altered granitic clasts; (ii) matrix-supported hematite-rich breccias, containing abundant hematite as clasts/replacements, but also as matrix/infill, and more intensely reworked clasts of granitic composition, in addition to rock-flour that may show fluidization textures; (iii) heterolithic breccias, containing hematite, altered granite and pervasively altered volcanic clasts occasionally displaying irregular, amoeboid-like margins, some of which are GRV-derived. The sample suite also contains all representative ore types (Electronic Appendix Fig. A1a–c, e), including high-grade bornite- and chalcocite-ores from the NW arm and middle parts of the deposit, respectively. In addition, sedimentary rocks comprising bedded clastic facies with hematite-rich, silty-sandstones with gradational or faulted contacts to hematite-rich breccia (Electronic Appendix Fig. A1f, g) were sampled from the upper part of the deposit in the SE lobe and from the sulphide-poor middle part of the deposit. Drillhole RD647 in the SE lobe is representative for thicker sequences of breccias with volcanic clasts. Those samples richest in hematite occur towards the centre of deposit and are characterized by the presence of different textural types of hematite cemented in a highly porous matrix consisting predominantly of finer hematite, minor amounts of other gangue components, and generally lack Cu(-Fe)-sulphides.

Although not continuously sampled across the 2 km vertical extent of the mineralisation, the deepest Cp-Py zone is sampled from the last 150 m in drillhole RD1988 whereas the uppermost Cp-Bn and Bn-Cc zones are sampled from ~300 m in drillhole RD2852A (Fig. 2a, b). In the latter, a sulphide-poor, Au-rich interval occurs underneath the Bn-Cc zone. A third, low-angle drillhole, RD2786A, intersecting deeper mineralisation from RD1988 was sampled as it contains one of the most diverse lithologies, including sedimentary rocks, granites, altered mafic dikes, etc. Both RD2786A and RD2852A drillholes intersect mineralisation with a pronounced polymetallic mineral signature (tennantite-dominant fahlores are present). A selection of representative elements are plotted from whole rock assays (data from BHP Olympic Dam; see also Ehrig et al., 2012) to show correlation with lithologies and sampled intervals (Fig. 2). Both Sn and W concentrations show a strong correlation with increasing Fe content in the SE lobe (Fig. 2d, e).

## 4. Methodology

One-inch diameter polished blocks were prepared and subsequently examined in reflected light microscopy and using a FEI Quanta 450 scanning electron microscope (SEM) equipped with a back-scattered electron (BSE) detector and an energy dispersive X-ray spectrometer (EDS). All instrumentation is housed at Adelaide Microscopy, The University of Adelaide. A small volume of electron probe data was collected to verify compositional zonation patterns using a Cameca SX-Five Electron Probe Microanalyzer operated at 15 kV and 20 nA. Details of standards, wavelengths and minimum limits of detection are given in Electronic Appendix B.

The main body of trace element data reported here was obtained by laser-ablation inductively-coupled plasma mass spectrometry (LA-ICP-MS) operating in spot analysis mode, using a RESOlution-LR 193 nm excimer laser microprobe coupled to an Agilent 7700cx Quadrupole ICP-MS. The analysed grains were pre-selected for LA-ICP-MS analysis based on textures, compositional zonation and relationships with co-existing minerals. Methodology followed established practices in the same laboratory (e.g., Ciobanu et al., 2013; Ismail et al., 2014; Xu et al., 2016). Details of operating conditions, reference standards and isotopes measured are given in Electronic Appendix B. Beam size varied from 29 to 51 μm, with 43 μm most commonly used for zoned hematite, depending upon the size and homogeneity of the analysed domains or grains. The reference materials BHVO-2G, GSD-1G and NIST-610 were used as external standards. Analysis time for each spot analysis was a uniform 60 s, comprising a 30-s measurement of background (laser-off), and 30-s analysis of the unknown (laser-on). All data reduction was performed using Glitter software (van Achterbergh et al., 2001). Internal calibration was achieved using ideal stoichiometric concentration of Fe in hematite as FeO in wt% (89.9810). For comparative purposes, concentrations below minimum limit of detection (< mdl) were treated as equal to that mdl value.

Element mapping by LA-ICP-MS was conducted using the same instrument by ablating sets of parallel line rasters in a grid across an area in the sample using laser repetition rates of 10 Hz and a fluence of 3.5 J/cm$^{-2}$. Beam sizes of 7 and, more commonly, 11 μm, and scan speeds of 7 and 11 μm/s respectively were chosen, resulting in the desired sensitivity of the elements of interest and adequate spatial

**Table 1**
Sample list and key characteristics.

| Deposit area | Drillhole | Sample | Depth (m) | Sulphide-zone | Key characteristics |
|---|---|---|---|---|---|
| SE lobe | RD1988 | RX7293B | 1618.5 | Cp-Bn | |
| | | RX7294GM/BW | 1768.7 | Py-Cp | |
| | | RX7295GM/BW | 1808.8 | Py-Cp | |
| | RD2786A | LCD02 | 1772 | Py-Cp | |
| | | MV023 | 1772.3 | Py-Cp | |
| | | MV024 | 1783 | Py-Cp | |
| | | LCD03 | 1785 | Py-Cp | |
| | | LCD04/MV025 | 1808.2 | Cp-Bn | |
| | | LCD05 | 1821.5 | Cp-Bn | |
| | | MV026 | 1826.2 | Py-Cp | |
| | | LCD06 | 1898.7 | Cp-Bn | Sedimentary facies |
| | | MV027 | 1908.1 | Cp-Bn | Sedimentary facies |
| | | LCD07 | 1930 | Cp-Bn | |
| | | MV031 | 1950.10 | Py-Cp | |
| | | MV032 | 1989.1 | Cp-Bn | |
| | | MV034 | 2062.3 | Cp-Bn | |
| | | MV028 | 2109.4 | Py-Cp | |
| | | LCD09 | 2133.4 | Py-Cp | Sedimentary facies |
| | RD2852A | RX6581 | 419.5 | Bn-Cc | |
| | | RX6583 | 488 | Bn-Cc | |
| | | RX6584 | 489.3 | Bn-Cc | |
| | | RX6585 | 490.4 | Bn-Cc | |
| | | RX6587 | 548.4 | Bn-Cc | |
| | | RX6601 | 617.2 | Bn-Cc | |
| | | RX6607 | 658.3 | Bn-Cc | |
| | | RX6609 | 679.5 | Bn-Cc | |
| | | RX6610 | 680.3 | Cp-Bn | |
| | | RX6612 | 682.3 | Cp-Bn | |
| | | RX6626 | 789.3 | Cp-Bn | |
| | RD647 | MV092 | 379.4 | Sulphide-poor | |
| | | LCD32 | 651.4 | Cp-Bn | |
| | | MV093A/B | 757.4 | Sulphide-poor | Granoblastic hematite filling vacuole(?) |
| | | MV094 | 819.7 | Sulphide-poor | |
| | | LCD35 | 821.8 | Sulphide-poor | |
| | RD1628 | LCD36 | 507.9 | Sulphide-poor | Fine-grained sedimentary fragments |
| | | LCD39 | 665 | Sulphide-poor | Fine-grained sedimentary fragments |
| | RD1629 | CLC109 | 705 | Sulphide-poor | Fine-grained sedimentary fragments |
| Middle | RU36-9867W1 | MV095 | 119.2 | Sulphide-poor | |
| | | MV096 | 145.8 | Sulphide-poor | |
| | | MV097 | 177.2 | Sulphide-poor | |
| | | MV099 | 349 | Cp-Bn | |
| | | MV100 | 384.8 | Py-Cp | |
| | RU49-8096 | CLC046 | 220.15 | Cp-Bn | |
| | | CLC047 | 226.15 | Cp-Bn | |
| | RU49-8097 | CLC050B | 93.5 | Bn-Cc | |
| | RD2765 | MV103 | 509.8 | Sulphide-poor | |
| | | MV104 | 583.5 | Sulphide-poor | |
| | | MV101 | 650.60 | Sulphide-poor | Sedimentary facies |
| | | MV105 | 665.30 | Sulphide-poor | |
| | RU34-8889 | CLC052 | 28.25 | Bn-Cc | |
| | RU34-8890 | CLC053A/B | 26.3 | Bn-Cc | |
| | | CLC054A/B | 26.75 | Bn-Cc | |
| | RU34-8891 | CLC055 | 34.5 | Bn-Cc | |
| | | CLC056 | 41.5 | Bn-Cc | |
| | Hand specimen | CLC057 | Underground (unlocated) | Cp-Bn | |
| NW arm | RU41-9882 | CLC201A/B/C | 62.85 | Cp-Bn | |
| | RU27-7551 | MV043 | 187.60 | Bn-Cc | |
| | | MV048 | 336.7 | Cp-Bn | |

resolution. Re-deposition during mapping was minimized by pre-ablating each line prior to data collection. A 10-s background acquisition was acquired at the start of each line and, to allow for cell wash-out, gas stabilization and computer processing, a delay of 20 s was used after each line. Spot analyses, with acquisition of 60 s signal (laser-on), were conducted on the standards at the start and end of each mapping run.

Individual line-profiles were processed together and compiled into 2-D images displaying the combined background-subtracted intensities for each element using the program Iolite (e.g., Woodhead et al., 2007).

## 5. Petrography and trace element distribution in granitophile-rich hematite

Petrographic aspects and LA-ICP-MS maps showing grain-scale trace element distributions for the U-(Pb)-W-Sn-Mo-rich hematite in the Olympic Dam orebody are shown in Figs. 3–12, and Electronic Appendix Figs. A1, 3–9. This type of hematite is identified in several textural categories with variable concentrations of U + Pb + W + Sn + Mo and with different concentrations of the individual elements relative to one another (Electronic Appendix C; see also below).

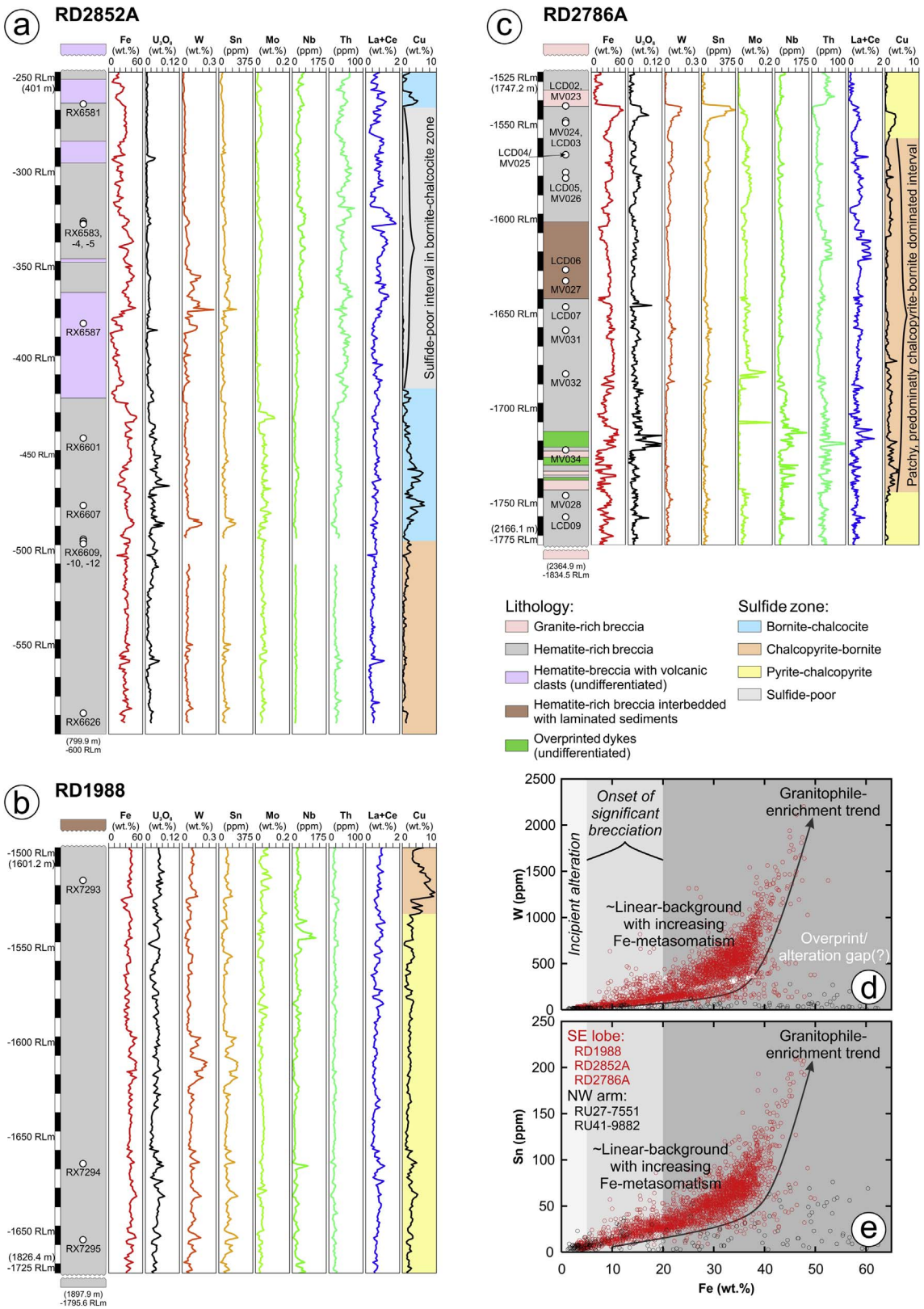


**Fig. 2.** Simplified drillhole logs showing schematic representations of profiles for selected elements and lithologies: (a) RD2852A; (b) RD1988; and (c) RD2786A. Whole-rock assay data was generally collected at ~1 m intervals. Note the locally good correlation between Fe and W, which is also mimicked by Sn enrichment. For comparative purposes, drillhole logs were projected on the absolute mine-grid depth (RLm) as both RD2852A and RD2786A are drilled sub-vertically. Whole-rock assay data for (d) W *vs.* Fe, and (e) Sn *vs.* Fe.

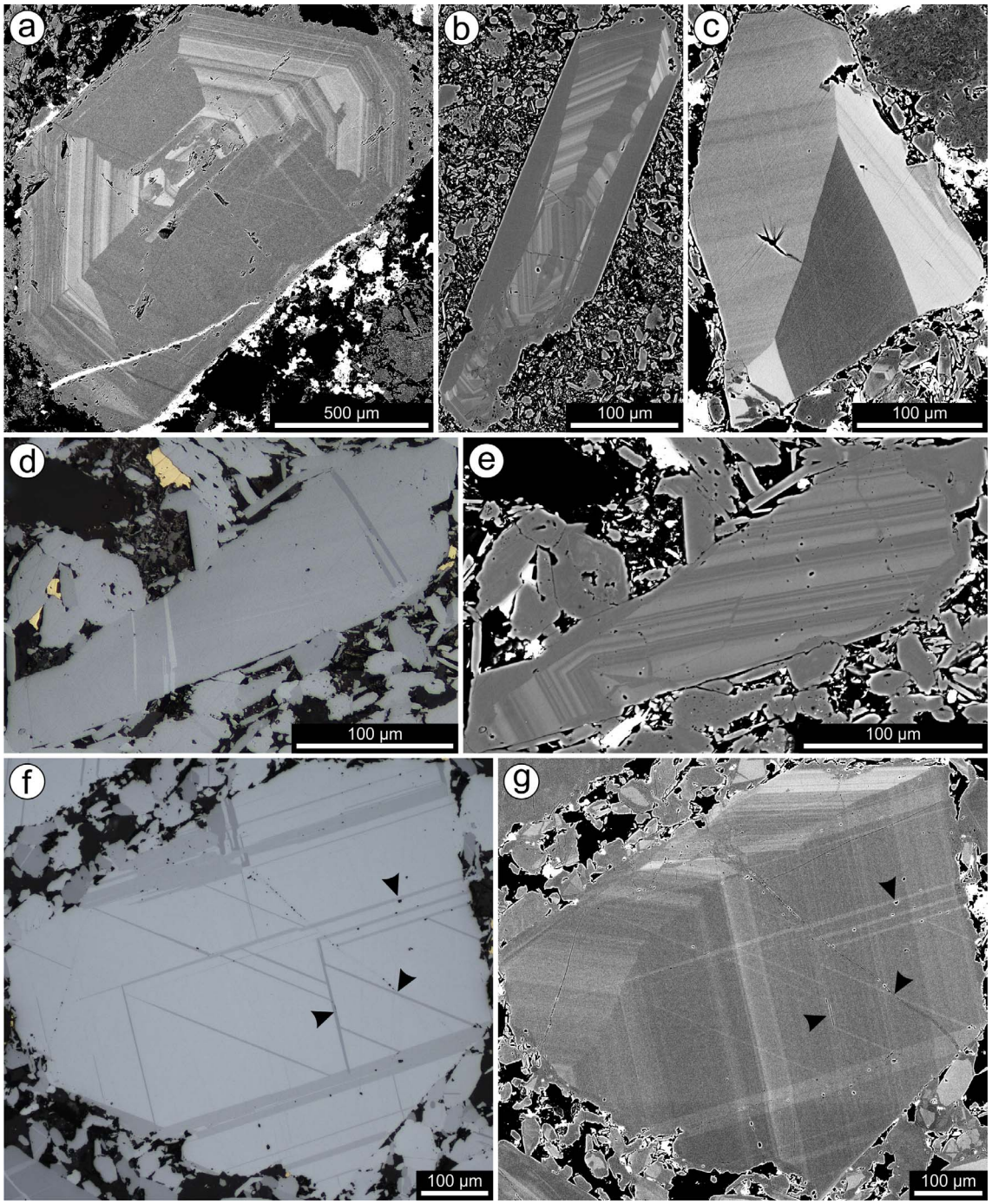


**Fig. 3.** Back-scattered electron (BSE) (a–c, e, g) and reflected light (d, f) microphotographs of oscillatory-zoned hematite showing types of zonation patterns and twinning. (a) Basal section of a euhedral, coarse-grained oscillatory-zoned hematite cross-cut by a barite veinlet (bright). Note the presence of darker domains (LA-ICP-MS maps in Fig. 9; sample was repolished). (b) Section approximately parallel to the *c*-axis showing a zonation pattern attributable to changes in the growth habit. (c) Reworked zoned hematite fragment (note slightly rounded edges), showing strong BSE-intensity contrast between different domains; note faint chemical-oscillations are still recognizable. (d–g) Relationships between sets of twins and zonation patterns. Note 3-sets of twins in (f), of which one has the direction of the chemical pattern, the other two are clearly visible on the BSE image. (e) Same grain as previous. Hematite overgrowths can be distinguished from the zoned domain. Set of twins, not recognizable in BSE image, cross-cut the zonation pattern and the overgrowth.

### *5.1. Categories of granitophile-rich hematite*

The distinct categories of granitophile-rich hematite are separated by prevailing textures as follows: (1) grain-scale oscillatory and/or sectorial zonation patterns – **zoned hematite** (Fig. 3); (2) hematite that replaces either siderite and/or ankerite **(carbonate replacement hematite**, 2a**),** or feldspars (**feldspar replacement hematite**, 2b) (Fig. 4a, b); (3) **granoblastic hematite** aggregates, which fill vugs in volcanic clasts (Fig. 5a; Electronic Appendix Fig. A1d); (4) **matrix fine-grained hematite** in volcanoclastic breccias (Fig. 4b); (5) **colloform/crustiform hematite** (Fig. 5c–e); and (6) secondary hematite replacing zoned hematite (**overprinted zoned hematite**).

All the above categories of hematite occur within hydrothermal breccias that also comprise other minerals, including Cu-(Fe)-sulphides and gangue phases, such as quartz, sericite, barite, carbonates, fluorite and accessory minerals, which vary in abundance. The accessory minerals are commonly represented by U- and REE-minerals, as well as others (e.g., zircon, rutile, and rare tourmaline). In addition, there are

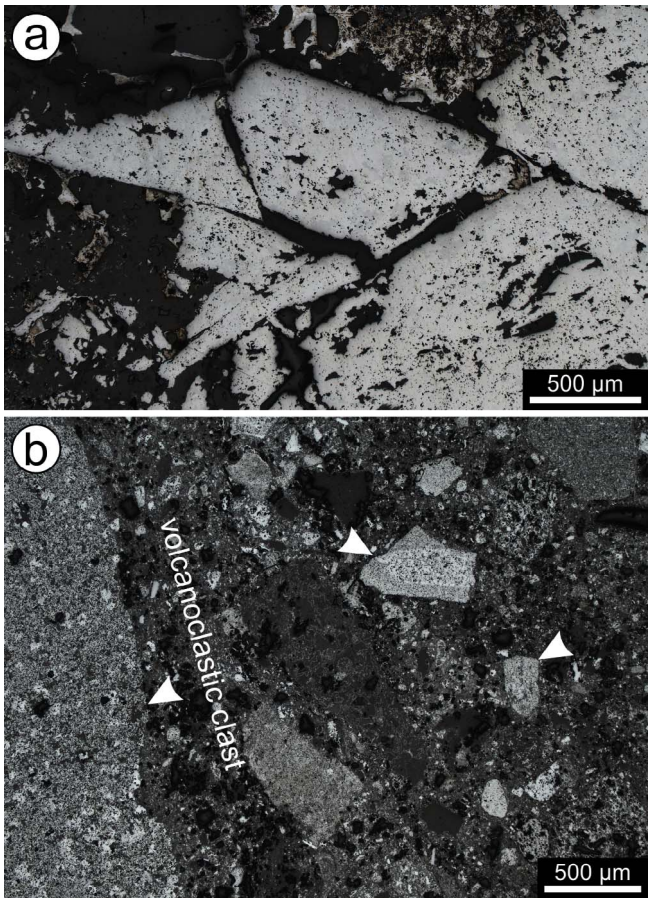


**Fig. 4.** Reflected-light microphotographs showing replacement hematite categories. (a) Carbonate replacement hematite showing fine-grained hematite filling coarse grains with rhombic, euhedral habit (inferred as carbonates). (b) Feldspar replacement hematite (arrowed), displaying core-to-rim zonation within volcanoclastic breccia; note also the fine-grained matrix hematite.

variable amounts of hematite poor in trace elements present in any sample containing the granitophile-rich hematite categories we focus on here. Such hematite is generally porous when replacing clasts or pre-existing minerals, occurs as single or lamellar aggregates within the breccia matrix, and often forms µm-sized, stubby grains as rims or inclusions within sulphides. Except for the stubby type, none of the other categories are readily distinguishable from some of the granitophile-rich categories studied here.

Several categories of granitophile-rich hematite are fine-grained aggregates that fill 'shapes', with morphology and/or characteristics attributable to pseudomorphic replacement of pre-existing minerals, either precursors to zoned hematite (carbonates, feldspars; categories 2a and b, respectively), or postdating an earlier generation of zoned hematite (overprinted zoned hematite; category 6). In the latter, relicts of non-replaced hematite can be occasionally recognised by their conspicuous zoning. Some categories of granitophile-rich hematite are not widespread across the deposit. For example, the carbonate-replacement type is presented only in samples from high-grade chalcocite ores in the middle part of the deposit (drillholes RU34-8889-91). This type stands out by its occurrence as fine aggregates that fill coarser (mm- to cm-sized) grains (Fig. 4a; Electronic Appendix Fig. A1e). In contrast, one of the widest ranges of texture is displayed by hematite from volcanoclastic breccias from the SE lobe (drillhole RD647; Figs. 4b and 5; Electronic Appendix Fig. A1d). These include fine-grained hematite filling subhedral grains with core-to-rim zonation suggestive of pseudomorphically replaced feldspar phenocrysts (category 2b; Fig. 4b), and aggregates of polygonal hematite occurring throughout mm-size clasts, hinting at vacuole filling (category 3; Fig. 5a). The latter hematite displays a 'basket-weave' texture (Fig. 5b). The nature of such a texture is the subject of nanoscale investigation.

Colloform hematite is fine-grained and occurs as crusts or radial aggregates around vugs, cementing earlier generations of lamellar hematite in the sericite ( ± Fe-rich chlorite) matrix (NW arm; drillhole RU27-7551; Fig. 5c–d), or within reworked breccia fragments elsewhere in the deposit. The colloform bands can develop concentric growth-zoning by subsequent cycles of precipitation, marked by differences in their width but otherwise homogeneous, and seemingly devoid of inclusions (Fig. 5f–e).

Zoned hematite (category 1), the main focus of the present study, is by far the richest in granitophile elements and has been studied throughout the entire deposit. Other categories, although they may have wider occurrence, are only included for purposes of comparison and assessment of the zoned category. Zoned hematite is most abundant within the SE-lobe, irrespective of the lithological complexity (sedimentary rocks, volcanoclastic breccias), and tends to decrease in abundance from deeper to shallower parts of the deposit. The sedimentary rock sequences in the SE-lobe display graded bedding and consist of silty, fine-grained sandstones with interstitial, fine-grained, unzoned hematite and sericite (Electronic Appendix Fig. A1f). In this case, the zoned grains occur along the stratification and are particularly abundant and coarser at boundaries between different grain size fractions. Zoned hematite is also common throughout the sulphide-poor interval in drillhole RD2852A in the SE lobe, which also contains Au-Cu alloys (Fig. 2a). Towards the deposit centre, zoned hematite is generally subordinate to its overprinted analogue (6). Notably, zoned hematite is present within samples from the contact between the ODBC and stratified sedimentary rock packages at shallow levels, where, in addition to zoned hematite, other textural types of (unzoned) hematite are recognised in the sedimentary stratification (Electronic Appendix Fig. A1g). Although the present study includes fewer samples from the NW-arm of the deposit, these samples nonetheless show the existence of zoned hematite as elsewhere in the deposit. Importantly, these samples include U-rich, high-grade bornite ore (Electronic Appendix Fig. A1b, h). In drillhole RU27-7551 from the NW arm, zoned hematite is rare but it can be also traced by the presence of overprinted varieties (6).

### 5.2. Zoned hematite – primary zonation patterns and their overprint

Zoned hematite varies in size, from a few µm to exceptional, mm-sized grains, and comprises isolated, single grains, as well as aggregates (Figs. 3 and 6). The most common variety of zoned hematite is represented by euhedral to subhedral, single grains with average sizes in the range of a few tens to hundreds of µm, with sections perpendicular, or along the *c*-axis (Fig. 3a, b). Fragments of crystals are also common, particularly in the sedimentary rocks (Figs. 3c and 6f). Polysynthetic twinning (Fig. 3d) is another common feature in zoned hematite, most often observed in coarser grains as one to rarely three sets of lamellae, where the latter is typical of equant grains (Fig. 3f). Occasionally, BSE images can reveal a correlation between chemical banding and twinning (Fig. 3e, g).

Zoning observable on the BSE images is represented by variations on the theme of oscillatory patterns at scales extending from a few tens of µm down to sub-µm size (Fig. 6). One common pattern features zonation correlated to grain morphology, expanding from the core to the margin whether in aggregates, in grains with prismatic-elongate habit (Figs. 3b and 6a), or within basal sections, as defined by their hexagonal or octagonal outlines (Figs. 3a and 6b). In many cases, the oscillatory pattern displays complexities such as difference in growth rhythms, suggesting either various growth cycles, or changes in the growth rate (Fig. 6a–c). Although less common, zoned hematite can show morphologies with a clast-like appearance and internal oscillatory patterns, which do not correlate with the grain outline (Figs. 3c and 6f). Within some grains, there are domains with darker or brighter

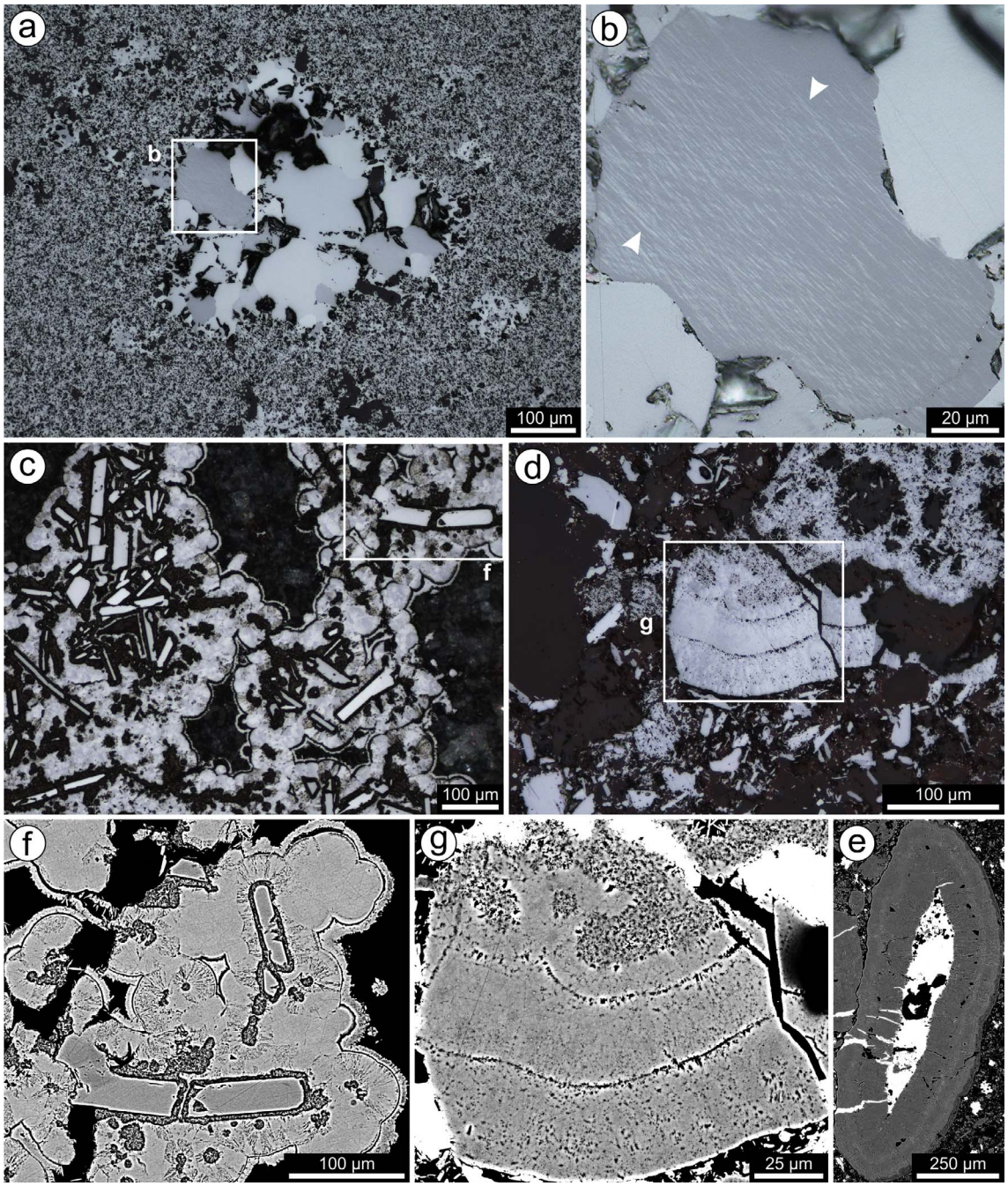


**Fig. 5.** Reflected light microphotographs (a–d) and BSE images (f–e) of other granitophile-rich hematite categories. (a, b) Granoblastic hematite filling vugs (vacuoles). In (b) note the basket-weave texture. (c–g) Colloform hematite from the NW arm and volcanics in SE lobe in (e). In (c) concentric bands surround lamellar hematite. (d) The bands are formed by fibrous hematite with radial arrangement relative to cores. (f, g) BSE images showing the presence of pores and no mineral inclusions present. (e) Concentric bands around a barite core.

intensities on BSE images that can be weakly zoned to unzoned, and either share coherent mutual boundaries with the oscillatory-zoned domains, or not (Fig. 3a–c). Such patterns may represent sectorial zoning, or, alternatively, reflect a new growth regime overprinting an initial grain (see below). Further complexity in the zonation patterns relates to grains that are affected by fracturing and development of porosity, with parts of the grain undergoing re-orientation of fragments displaying zonation followed by replacement (Fig. 6b, c; see below), or, in other examples, a second cycle of rhythmic growth (Fig. 6a, d).

Throughout the deposit, most primary zonation patterns in zoned hematite are variably overprinted, sometimes resulting in partial to complete obliteration of the primary textures (Fig. 7a). Many samples contain examples of both partially unaltered and overprinted zoned hematites coexisting in the immediate vicinity of one another. Overprinting processes are reflected in the generation of a wide variety of 'new' textures (Fig. 7). New core-to-rim patterns can be inferred from reworked domains where a darker shade on BSE images correlates with the presence of pores (Fig. 7b). Exceptionally, tiny blades of REE-fluorocarbonates occur throughout such grains. Overgrowths, consisting of acicular aggregates of hematite depleted in granitophile elements, are observed around zoned hematite (Fig. 7c). Boundaries that display intense darkening on BSE images (depletion in granitophile elements) are considerably common. These are often associated with pores, some of which may retain µm to sub-µm inclusions in them (Fig. 7d, e). The most commonly observed inclusions are U( ± Pb)-minerals (uraninite, rarely coffinite), W-minerals (scheelite or

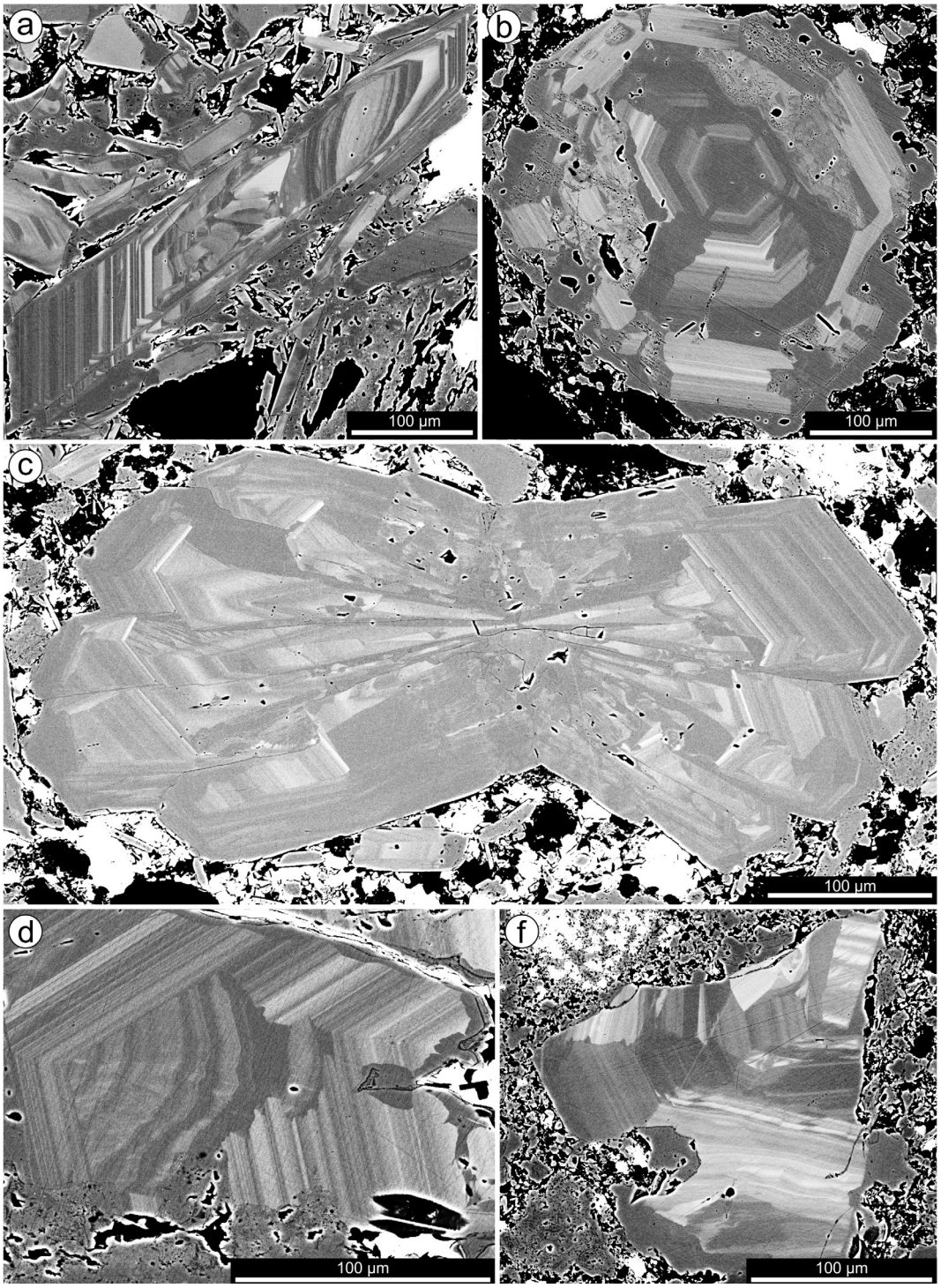


**Fig. 6.** BSE images showing complex oscillatory zoning patterns and incipient overprint. (a) Core to rim zonation in single grain cut parallel to the *c*-axis. (b) Core-to-rim zonation in octahedral basal section. Note parts of the grain showing reworking of zonation in areas marked by porosity. (c) Typical aggregate of oscillatory zoned hematite. Note zonation outlines growth in two directions (twins?) outwards from the middle part. (d) Detail of aggregate shown in Fig. 9b displaying two oscillatory zoning cycles marked by reversal growth direction. Although the inward cycle is an overprint, U and W are preserved. (f) Oscillatory zoned-grain with a 'clast'-like appearance.

ferberite), cassiterite, as well as REE-minerals (commonly monazite) or rare Nb( ± Ti)-oxides.

### 5.3. Grain-scale trace element distribution – LA-ICP-MS maps

The correlation between the textures described above and trace element associations are illustrated by grain-scale element maps (Figs. 8–12; Electronic Appendix Fig. A3–9). The complexity of zonation patterns, in terms of inter-element correlations, within zoned hematite is highlighted on Figs. 8–10. In all cases, there is an intrinsic correlation between the zonation visible on BSE images and the presence of granitophile elements, in which the brightest areas are enriched in U(+Pb), and/or W, or to a combination of granitophile elements in different proportions.

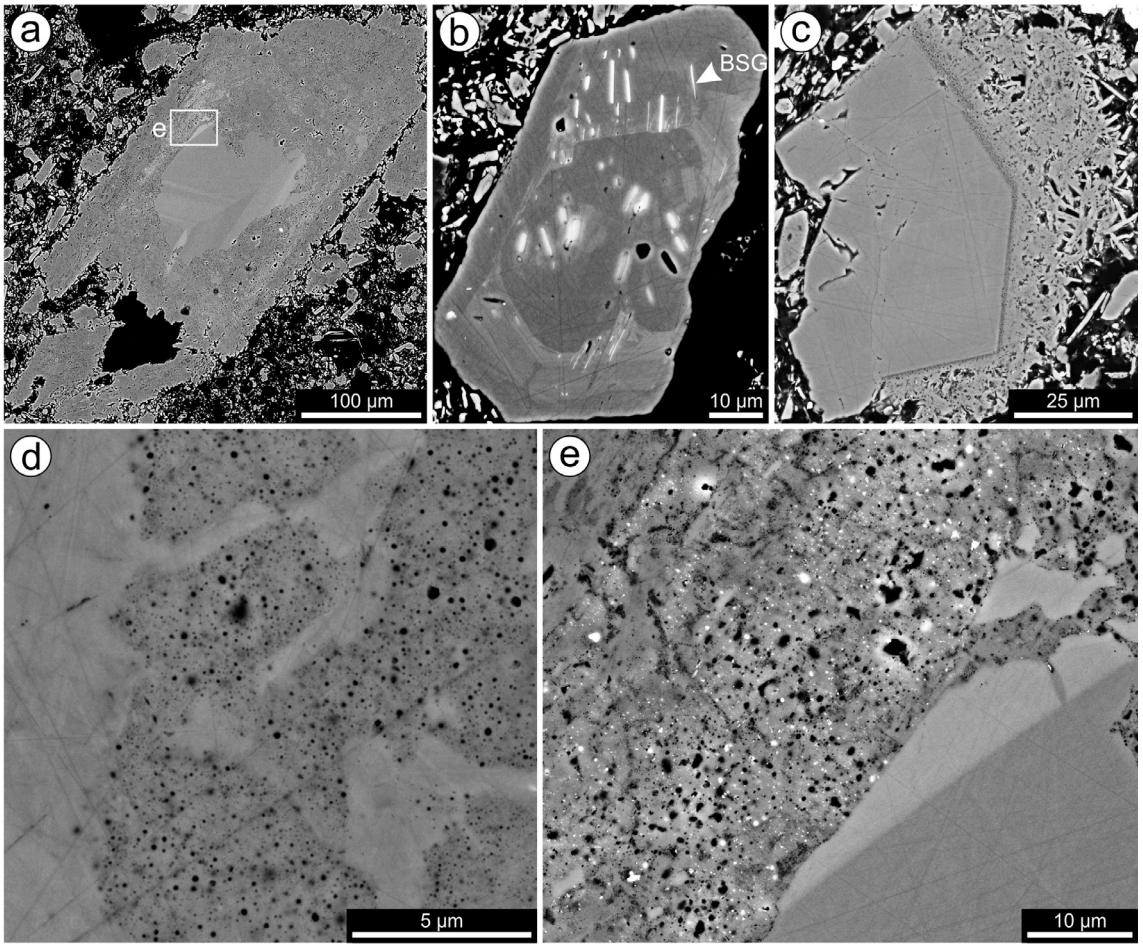


**Fig. 7.** BSE images showing aspects of zoned hematite overprint. (a) Advanced replacement marked by pores, darkening and irregular grain margins. Zoned relict recognizable in the core. (b) Reworking of zoned hematite with recrystallised core and REE-fluorocarbonates from bastnäsite-synchysite group (BSG) as lamellar inclusions. (c) Replaced zoned hematite with outwards lamellar overgrowth. (d-e) Details of patterns resulting during overprint in (a) showing high porosity (d) and inclusions attached to pores (e).

*5.3.1. Element maps for zoned hematite*

Zoned hematite grains from the middle part of the deposit are represented by the element maps shown in Fig. 8 (sample CLC046). This grain displays distinct inter-correlations between granitophile elements throughout different domains of sectorial and oscillatory zonation. In the sectorial domain, moderate concentrations of W correlate with highest concentrations of Mo, but the brightest areas on the BSE images correlate with highest U + Pb + W + Sn. The margins of the oscillatory-zoned grain show an inverse correlation between W + Sn (rich) and U + Pb (poor). In all maps of zoned hematite, there is a strong correlation between U and radiogenic Pb ($^{206}$Pb and $^{207}$Pb). The brightest areas on the zonation patterns are therefore those with high U (+Pb), followed by W, whereas areas enriched in Sn or Mo can appear comparatively dark on the BSE images.

Partial overprinting of oscillatory-zoned hematite from the chalcocite-bornite zone of the mineralisation in the SE lobe is shown by element maps in Fig. 9 (sample RX6607). One of the most remarkable aspects revealed by mapping is the decoupling between granitophile elements in domains that show overprinting (recognizable by a darkening on BSE images; Fig. 9). In this case, the area is strongly depleted in W + Mo yet shows unchanged zonation with respect to Sn. Uranium, although not so enriched in this grain, and also $^{206}$Pb (not shown), partially correlates with Sn. Oscillatory zonation with respect to Nb towards the margin is retained but the element is locally depleted within the core. Other elements (not shown) that mimic the distribution of Sn (unchanged zoning), or W (changed zoning) are Al + V and Mn + Co (very low), respectively. Reincorporation of granitophile elements such as W and U(+Pb) into secondary oscillatory zonation patterns (Fig. 6d) within the same grain is also observed in aggregates with intensive overprinting within the same sample (Fig. 9b).

Zoned hematite in samples from the chalcopyrite-pyrite zone in the deepest part of the SE lobe (RX7294) displays oscillatory zonation patterns with good spatial correlation between all the granitophile elements (Fig. 10). In addition, the zonation includes REE (e.g., Ce, Y), also overlapping with areas of the grains in which Th is present. Such elements are, however, only present at low concentrations in zoned hematite within the orebody. Other elements (not shown on the maps) present within the zonation pattern are Mn, V and Al (enriched in the grain margins), Ga, As, and Nb (low concentrations but nonetheless zoned).

Element maps of hematite grains from sulphide-poor intervals in the SE lobe, intersected by drillhole RD2852A (Fig. 11; sample RX6584) show some of the most complex trace element distributions. The mapped grain fragment displays a weak zonation on the BSE image, in which a darker band separates distinct inner and outer domains with only weak contrast between one another. The inner domain shows enrichment in Sn, W, Al and Ga (generally not distinctly zoned in other mapped grains), with scattered U, $^{206}$Pb, Mo and Sb (noisy). Manganese is enriched in parts of the inner domain in which other elements are relatively depleted. Uranium, $^{206}$Pb, Mo and Al are at their maximum concentrations in the outer domain. The darker band is characterized by a strong enrichment in As and Sb, also correlating with Cu, suggesting the presence of these metals within the hematite grain.

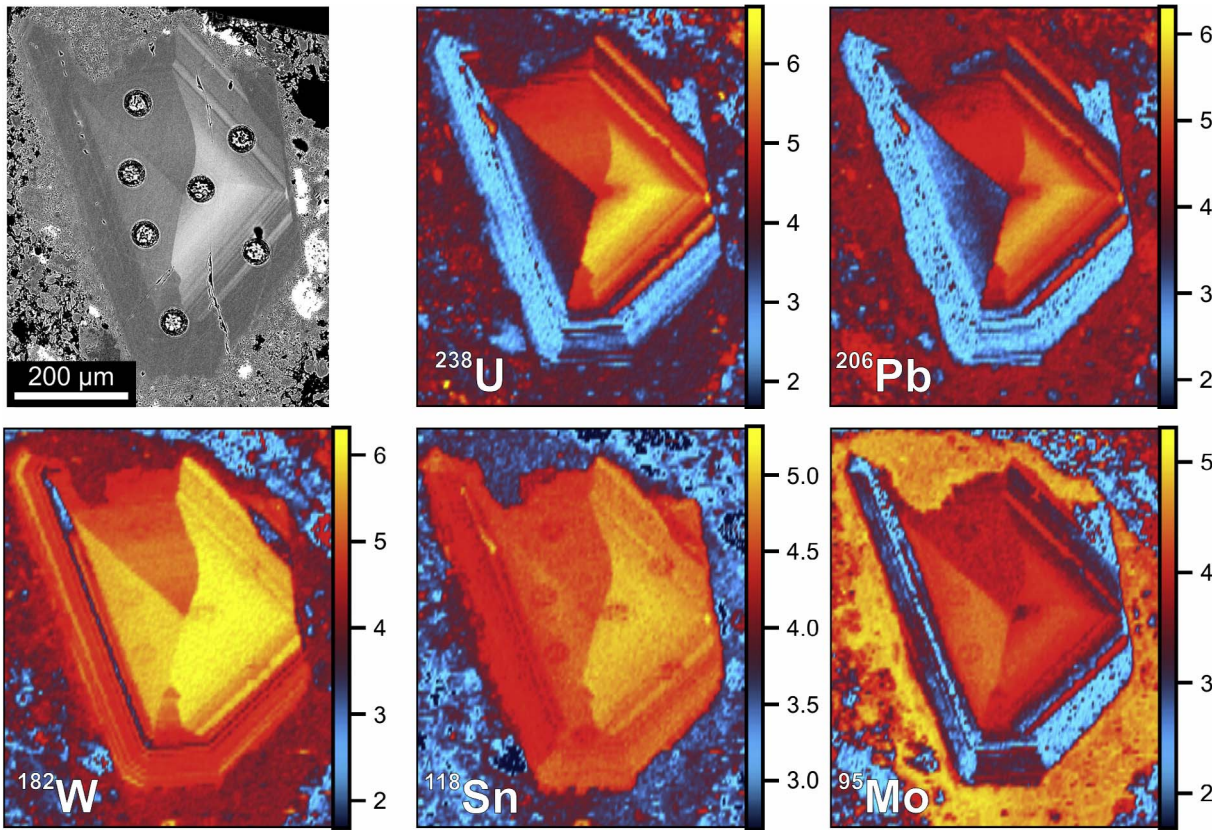


**Fig. 8.** LA-ICP-MS maps of zoned hematite (sample CLC046, RU49-8096). Scales in counts-per-second (logarithmic scale, $10^n$). Spots on the BSE image (upper left) are previously acquired laser-ablation spot analysis.

*5.3.2. Element maps for other categories of granitophile-rich hematite*

Element maps (Fig. 12a) of granoblastic hematite from a volcanic clast shown in Fig. 5a (sample MV93A, SE lobe) show Sn as the granitophile element with highest concentration whereas U, W and Mo (not shown) are much lower and have a slight inverse correlation to Sn. Highest concentrations are observed for V towards the margin of the vug, inversely correlating with Nb (inner part). Titanium shows a positive correlation with Sn, albeit with two areas that are very high. LREE (Ce) (not shown) are also present throughout the middle part of the aggregate. Interestingly, Zn is present outside the margin of the vug, and correlates with Mn (not shown).

Colloform hematite from the NW lobe (sample MV048) shows complex distribution patterns (Fig. 12b) that reproduce the concentric zoning observed on BSE images. The darkest areas on the BSE image comprise fine-grained mixtures of Fe-hydroxides and silicates (depleted in Fe, enriched in Si and Al, not shown). The brightest bands correlate with highest concentrations of $^{206}$Pb, U, Th, HREE (Yb), as well as Mo and to a lower extent Sn and W (not shown). This is the only case we have mapped which shows Pb at higher concentrations than U (see below). In contrast, the darkest areas on BSE and their margins are richer in LREE (Ce). An interesting feature is the presence of As at relatively high concentrations throughout the concentric banding. Other elements not shown on the figure (Sb, Cu, Zn and Ga) partially mimic the As distribution.

## 6. Compositional data

### 6.1. Electron probe microanalysis

Although the present work has used LA-ICP-MS methods to provide quantitative trace element data for hematite, a limited EPMA study was carried out to confirm the presence of lattice-bond granitophile-elements in zoned hematite and to assess, at the smaller scale of the microprobe beam, the variation within a single, particularly U-rich, zoned grain. Representative EPMA analyses of bright and dark domains on the BSE image of this grain from the SE lobe (RD2852A) are presented in Fig. 13. EPMA data are provided in Electronic Appendix D. Observed zonation patterns reflect bi-modal alternation between granitophile-rich hematite and end-member hematite (Fig. 13b). Concentrations of MgO, $Al_2O_3$, $SiO_2$, $P_2O_5$, CaO, $TiO_2$, $V_2O_3$, $Cr_2O_3$, MnO, NiO, ZnO, $ZrO_2$ and $Nb_2O_5$ are negligible in both bright and dark domains, mostly below their respective limits of detection and rarely exceeding 0.1 wt%. Uranium concentrations can be high, reaching a maximum concentration of 2.33 wt% $UO_3$, equivalent to 0.013 atoms per formula unit (apfu). Spot analyses with higher U are accompanied by variable, but sometimes higher, concentrations of W (in this case up to 1.61 wt% $WO_3$ or 0.011 apfu, Fig. 13b). Even though concentrations of both U and W are typically higher within brighter domains on the BSE image, Fig. 13b indicates that a degree of decoupling of the two elements has occurred within some zones. Generally in the present sample suite, most of the measured elements in zoned hematite are subordinate to W. Irrespective of spot location within the zoned grain, Sn concentrations consistently exceed the minimum limit of detection, albeit at low concentrations, reaching a maximum of up to 0.14 wt% $SnO_2$. Molybdenum is also present, reaching a maximum of 0.18 wt% $MoO_3$, although normally subordinate to other granitophile-elements, and decreasing towards grain margins.

### 6.2. LA-ICP-MS trace element data

This study comprises 1037 spot analyses of zoned hematite, 194 of *carbonate-replacement hematite*, 96 analyses of replaced zoned hematites, 50 of colloform hematite, 22 of granoblastic hematite, including the finer hematite matrix, and 12 analyses of *feldspar-replacement*

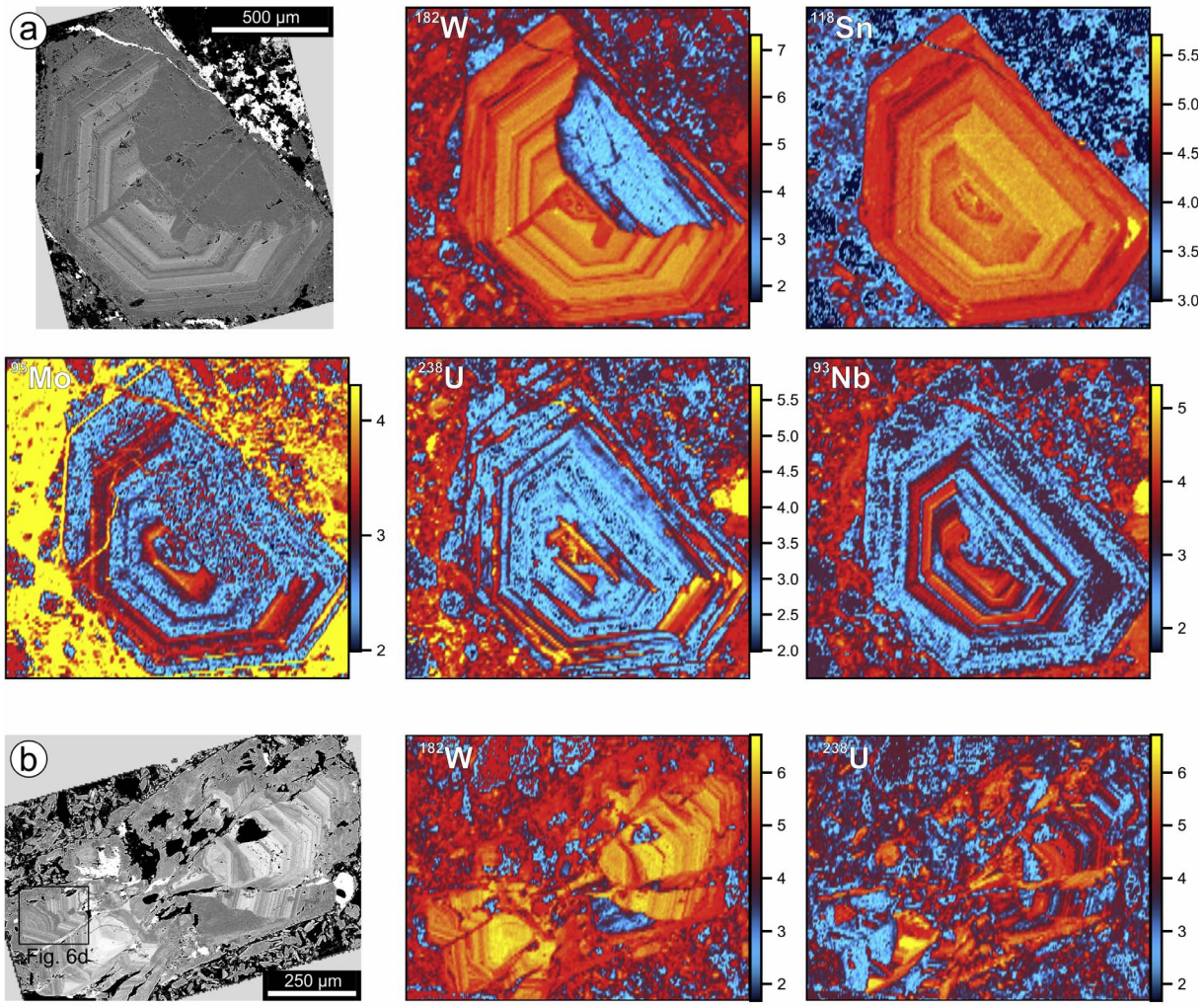


**Fig. 9.** LA-ICP-MS maps of two zoned hematite grains (a, b) in sample RX6607 (RD2852A). Scales in counts-per-second (logarithmic scale, $10^n$). BSE images of mapped areas are shown for comparison.

*hematite*. The study is intentionally biased towards coarser, granitophile-rich grains that could be readily analysed by LA-ICP-MS using larger spot sizes. For all textural types, time-resolved LA-ICP-MS profiles show smooth, flat signals for the granitophile elements and others, indicating homogeneous distributions of these elements in the ablated volumes (Electronic Appendix Fig. A2). There are, however, examples of noisier signals that attest to the presence of discrete inclusions of phases containing Cu, REE, Th, Nb, W, Sn, U and Pb. These spot analyses were either excluded from the data presented, or the integrated time-intervals were reduced to avoid undue influence from these inclusions. Summary statistics for the dataset are presented in Electronic Appendix C; ternary and bivariate scatterplots for the data are shown in Figs. 15 and 16, respectively.

### 6.2.1. Granitophile elements: U(-Pb), W, Sn, Mo and Th

Across the deposit, hematite from the categories considered here, regardless of textural type and lithological association, is characterized by measurable concentrations of U, W, Sn and Mo. Lead is also measured within such hematites, in most cases as radiogenic Pb (see below). Normally, the concentrations of granitophile elements in zoned hematite vary in the range of some hundreds to a few thousands of ppm, following the order of abundance $W \gtrsim Sn \gtrsim U \gtrsim Mo$, not uncommonly with values across several orders of magnitude, particularly for U. Typical concentrations of these elements vary in the ranges of 20–370 ppm U, 1800–8900 ppm W, 300–1100 ppm Sn and 50–330 ppm Mo. Molybdenum concentrations are, in general, more consistent than those of U and display more limited variation, albeit at lower absolute concentrations. Despite U, Sn and Mo being typically subordinate to W, they can reach significant concentrations in individual spot analyses (10000–20000 ppm), and in rare cases, may even be present at higher concentrations than W (e.g., up to ca. 27000 ppm Sn and ca. 12000 ppm Mo).

A series of cumulative plots (Fig. 14) depict the variation in the concentrations of granitophile elements in hematite, commonly over several orders of magnitude within individual samples, or across sampled drillcore intervals. Neither the range of absolute values nor their variation show any significant differences with respect to vertical position in the deposit or sulphide zone (i.e., concentrations are broadly comparable in zoned hematite from different sulphide zones).

The zoned hematite clearly displays the highest maximum and mean concentrations of granitophile elements, followed closely by the carbonate-replacement category (600–1100 ppm U, 330–680 ppm W, 610–1200 ppm Sn, and 30–50 ppm Mo), and then by overprinted zoned hematite (490–960 ppm U, 120–440 ppm W, 120–300 ppm Sn, and 20–50 ppm Mo). The carbonate replacement category, restricted to the middle part of the deposit, displays a relatively consistent composition across the dataset, without the marked variance shown by zoned hematite (compare Fig. 14a, c). Particularly, U concentrations in carbonate replacement hematite show markedly less scatter than U concentrations in zoned hematite (Fig. 14c).

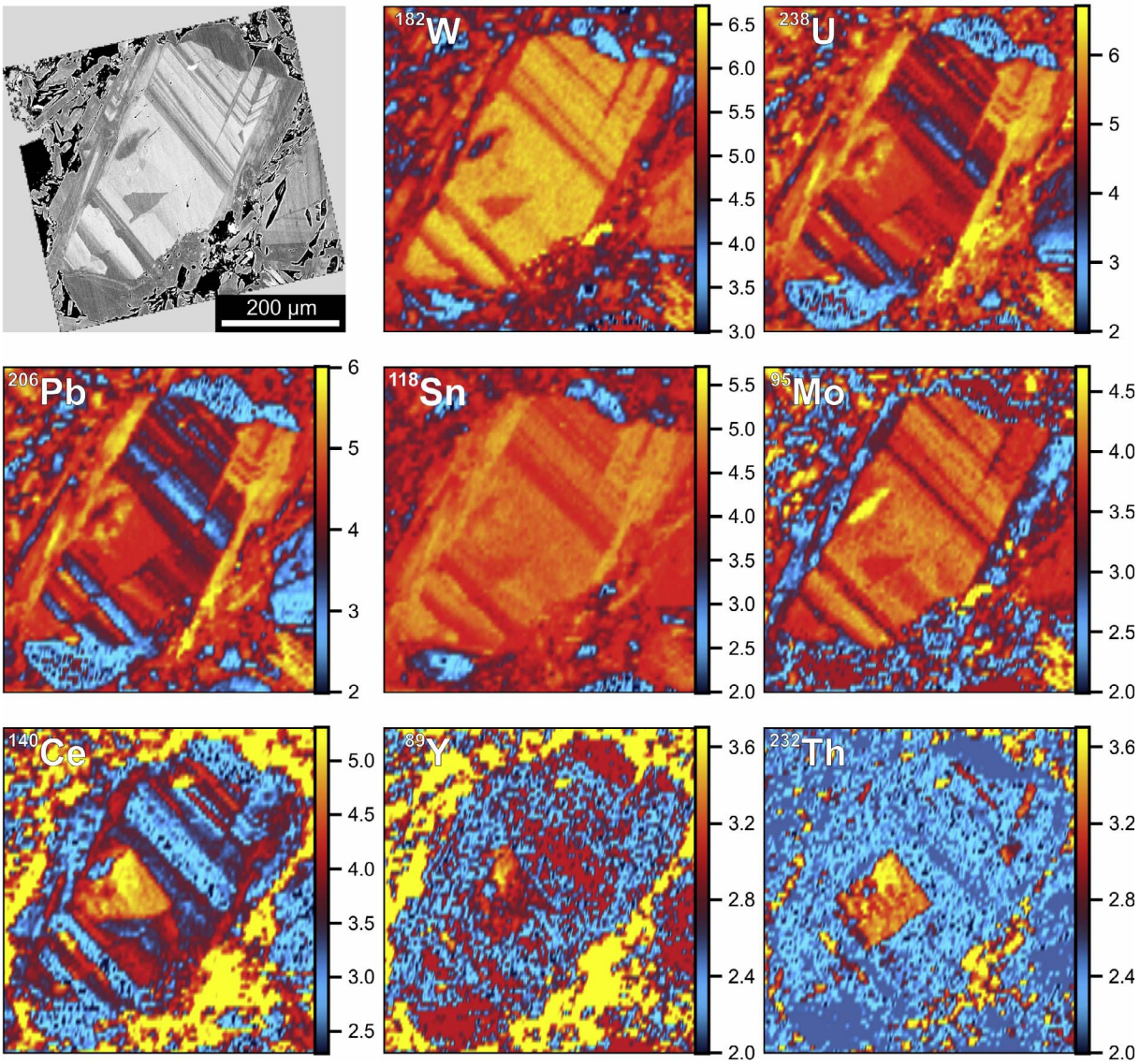


**Fig. 10.** LA-ICP-MS maps of zoned hematite (sample RX7294, RD1988). Scales in counts-per-second (logarithmic scale, $10^n$). BSE images of mapped areas are shown for comparison.

Despite the lack of marked differences in concentrations between sulphide zones, the dataset shows that zoned hematite from the SE lobe has a particularly pronounced granitophile signature. Whereas U, Sn and Mo concentrations in zoned hematite are comparable across the deposit, W is distinctly more enriched in the SE-lobe relative to the central area or the NW-arm. This feature is seen on ternary diagrams for granitophile elements (Fig. 15). A discrimination between other textural types in terms of the relative abundance of these elements can also be seen.

Other textural types, although generally exhibiting lower concentrations of granitophile elements, can nevertheless be characteristically enriched in one of these elements. Tin concentrations, for example, can reach up to 200 ppm in granoblastic hematite whereas U, W, and Mo are < 10 ppm (Fig. 14c).

Variation in the concentrations of granitophile elements in hematite is exemplified by a plot of U *vs.* Mo + Sn + W (Fig. 16a). The considerable spread in zoned hematite and lesser variance in other textural types can be seen clearly. Concentrations of Th are much lower than U or the other granitophile elements. The element is, however, distinctly enriched (sample averages of up to ~150 ppm) in carbonate replacement hematite and overprinted hematite (typical ranges of 60–120 and 90–140 ppm Th, respectively). Fig. 16b shows a positive but rather weak correlation between Th and U in zoned hematite, and a stronger correlation among the other categories. Concentrations of Th discriminate colloform hematite (6–15 ppm) from zoned and granoblastic hematite (< 1 ppm). Radiogenic Pb, the product of U and Th decay, is also present in hematite, at concentrations that can exceed 1000 ppm. A strong correlation is seen between U and Pb (Fig. 16c), where Pb corresponds to an estimate the total lead amount calculated from the individual $^{206}$Pb, $^{207}$Pb and $^{208}$Pb abundances. Notably astray from the main correlation, however, is the colloform hematite with comparatively high Pb concentrations and lower U/Pb ratios, suggesting a different, or later formation, in which $^{206}$Pb, $^{207}$Pb and $^{208}$Pb from *in situ* decay of U and Th is supplemented by additional radiogenic lead, possibly migrated from the decay of U- and Th-bearing minerals unable to retain Pb within their structures.

### 6.2.2. *Rare earth elements and yttrium*

Despite the abundance of other REE- and Y-bearing minerals at OD, hematite is a significant host for REY. ΣREY (the sum of all REE, La to Lu, and Y) varies over 5 orders of magnitude, from fractions of a ppm, to as much as 1000 ppm (Fig. 16d, e). ΣREY values for zoned hematite span the entire range but are, on average, among the lowest of all categories, together with granoblastic hematite, which contains 1–12 ppm

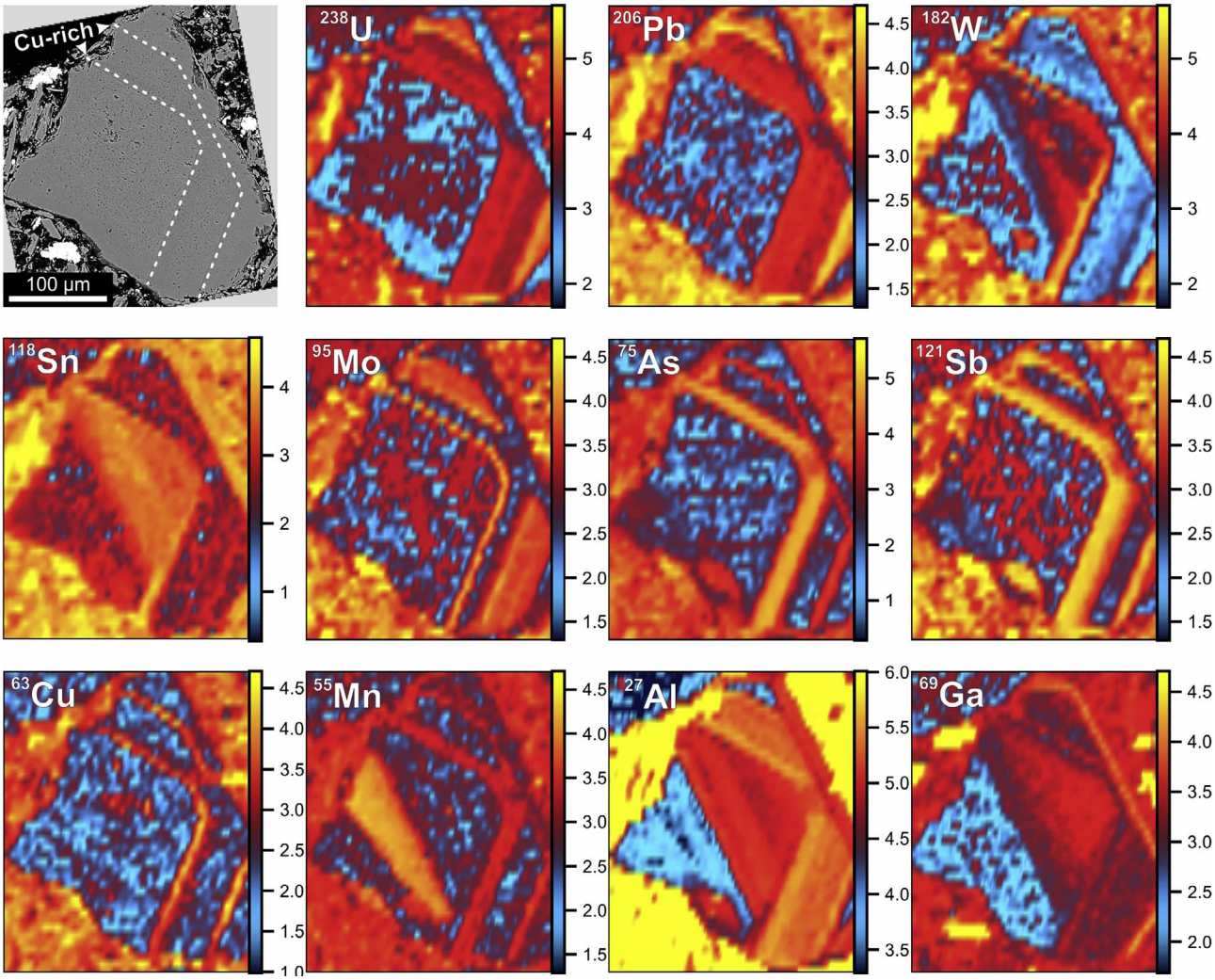


**Fig. 11.** LA-ICP-MS maps of zoned hematite (sample RX6584, RD2852A). Scales in counts-per-second (logarithmic scale, $10^n$). BSE images of mapped areas are shown for comparison.

ΣREY, and rarely surpasses 150 ppm. Other textural types commonly have higher and more consistent ΣREY than zoned hematite (e.g., colloform hematite, which can reach up to ca. 300 ppm). A comparison of chondrite-normalized REY-fractionation trends for different categories is shown in Fig. 17. Different textural types of hematite can be distinguished based on their REY-patterns, however some types display marked variability within and between samples (particularly true for granitophile-zoned hematite).

The zoned hematite grains which are relatively enriched in ΣREY generally show REY-fractionation patterns defined by LREE-enrichment, concave trends and smooth slopes, which flatten or become slightly, but steadily enriched in HREE (Fig. 17a). Such a trend is, however, more common in zoned hematite from the SE-lobe at depth, although, individual samples from other localities may contain grains showing similar trends. More commonly, however, zoned hematite contains very low amounts of ΣREY, with several REE at or below their respective minimum limits of detection, producing erratic fractionation trends that are accentuated on logarithmic plots. One common trend (Fig. 17b) shows a sinuous fractionation with slight LREE-enrichment and a pronounced negative Y-anomaly. One specific example is highlighted on Fig. 17b (sample MV031) which depicts a smooth, LREE-enriched trend with a marked positive Eu-anomaly, atypical for zoned hematite across the deposit. Less commonly, zoned hematite may also feature distinct HREE-enrichment (Fig. 17c), a pattern that may be accompanied by more to less pronounced, negative Eu-anomalies.

Other textural types show chondrite-normalized REY-fractionation trends that can be distinguished from those of zoned hematite. Carbonate-replacement hematite (ΣREY: 25–45 ppm) features fractionation trends characterized by slight LREE-enrichment, negative Eu-anomalies and an overall continuous HREE enrichment (Fig. 17d), similar to patterns observed in some overprinted hematites, which also have comparable ΣREY (30–55 ppm). Hematite replacing feldspar shows fractionation-patterns characterized by slight LREE-enrichment and otherwise smooth patterns with small positive Eu- and negative Y-anomalies (Fig. 17e), resembling and in the same range as fine-grained hematite matrix, whereas granoblastic hematite shows less-enriched trends. Colloform hematite displays fractionation patterns characterized by smooth, flat slopes with slight positive Eu- and negative Y-anomalies (Fig. 17f), albeit with subtle differences between individual samples.

### 6.2.3. *Arsenic and antimony*

Arsenic and Sb are both measured in all textural types of hematite, varying in concentrations (Fig. 16f), typically with As > Sb, but within similar concentration ranges. Typical ranges for zoned hematite are 2–26 ppm As, and 2–13 ppm Sb, although higher concentrations are measured in some spots. Zoned hematite from the NW arm and deposit centre appear to have only moderate concentrations of As and Sb compared to most analyses of zoned hematite from the SE lobe. Typically, colloform hematite shows characteristically high As and Sb, as does the matrix hematite. In general, As and Sb concentrations correlate positively for most textural types, although colloform hematites do not

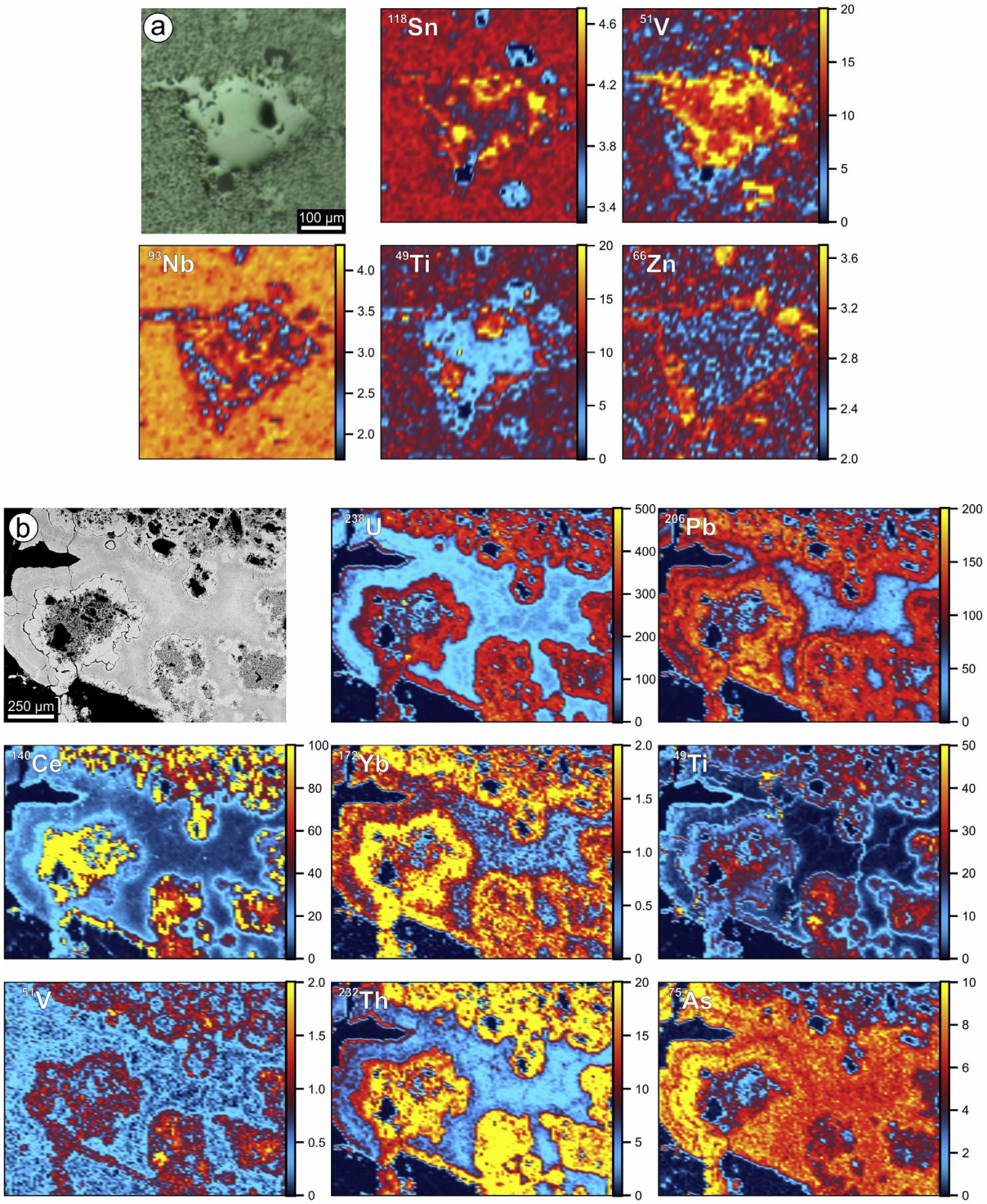


**Fig. 12.** LA-ICP-MS element maps of (a) granoblastic hematite (sample MV093, RD647) and (b) colloform hematite (MV048, RU27-7551). Scales in counts-per-second (logarithmic scale, $10^n$). $^{49}$Ti and $^{51}$V on (a), and $^{238}$U, $^{206}$Pb, $^{140}$Ce, $^{49}$Ti, $^{232}$Th and $^{75}$As on (b) are linearly scaled (n·1000). Upper left images of the ablated area are an optical micrograph (a) and BSE image (b).

follow this trend and appear to be uncorrelated (relatively constant As concentrations but Sb varying over ca. 1–2 orders of magnitude).

### 6.2.4. Transition metals: Cr, Mn, Co Ni, Cu and Zn

Increased Ni, Cu and Zn concentrations show a strong positive correlation with higher As + Sb (Fig. 16f), raising the possibility of sulphide inclusions, which are common in replacement and overprinted textural types. Some zoned hematites from the SE-lobe show comparatively low concentrations of Ni + Cu + Zn despite higher As + Sb. Zoned hematite from the NW arm and deposit centre appear to have only moderate concentrations of Ni, Cu and Zn compared to most analyses of zoned hematite from the SE lobe.

Chromium, Mn and Co do not appear to be particularly enriched in OD hematite. All three elements are generally found at concentrations < 100 ppm, with Mn > Co. Among the different textural types, zoned hematite contains the lowest Cr, Mn and Co contents (together

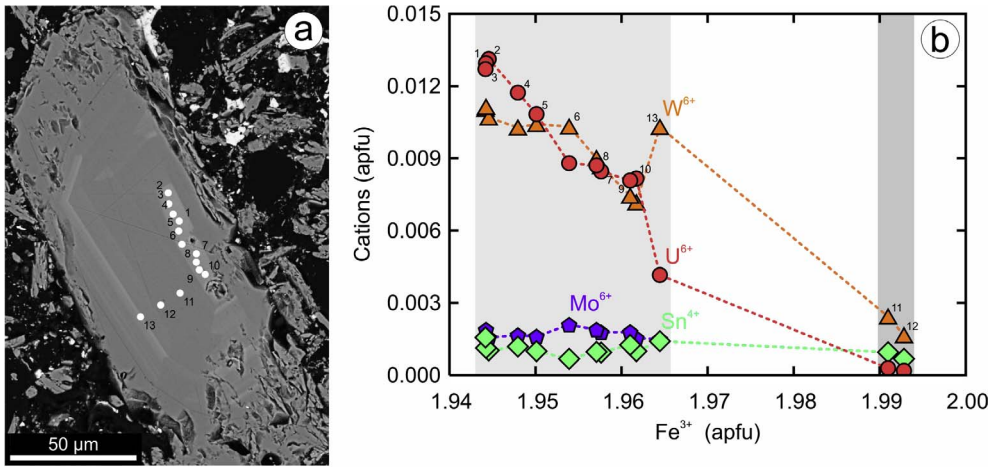


**Fig. 13.** (a) BSE micrograph of U-rich zoned hematite (sample RX6583, RD2852A) and location of spots analysed by EPMA (numbered white dots). (b) Compositional variation between different domains within the zonation pattern depicted by $Fe^{3+}$ *vs.* $U^{6+}$, $W^{6+}$, $Sn^{4+}$ and $Mo^{6+}$ in atoms-per-formula-unit (apfu). Hematite formulae calculated based on 3 apfu O.

commonly < 20 ppm), whereas other types contain higher concentrations. Chromium does not correlate with other transition metals, while Mn and Co appear to be slightly correlated, with both showing concentrations in comparable ranges and increased concentrations in carbonate replacement hematites (28–62 ppm Mn, 15–27 ppm Co) and overprinted hematites (40–92 ppm Mn, 12–21 ppm Co).

#### 6.2.5. *High field strength elements: Sc, Ti, V, Zr(-Hf) and Nb(-Ta)*

Compared to the granitophile elements, concentrations of HFSE are not particularly high in zoned hematite. They can, however, reach significant concentrations in other textural categories, such as in replacement-types, granoblastic and colloform hematite. Typically, V is present in zoned hematite at concentrations < 10 ppm and Nb is present at somewhat higher concentrations. There is however a marked increase in the Nb concentration in zoned hematite from volcanics in the SE lobe (up to ~2800 ppm), although individual samples from the middle part of the deposit (up to ~2000 ppm) and from the NW arm (up to ~1800 ppm) can also reach considerable amounts. Both elements are, however, clearly enriched in other categories relative to zoned hematite, reaching up to a few hundreds of ppm V, and a few thousands of ppm Nb: 440–1400 ppm Nb and 280–390 ppm V in carbonate replacement hematite, and 700–2700 ppm Nb and 100–200 ppm V in replaced zoned hematite. Niobium correlates positively with Ti + V (Fig. 16g) and a good correlation between V + Nb and Sc + Ti + Y + Zr is also seen (Fig. 16h). While the majority of zoned hematite shows significant scatter irrespective of location, carbonate-replacement and overprinted zoned hematite can be effectively discriminated by their particular HFSE signatures, plotting generally together as a group, or at least close to one another. Irrespective of textural type, concentrations of Nb are mimicked by Ta, even if at low concentrations, giving good correlations albeit with considerable scatter.

Typically, zoned hematite is poor in Ti, contrasting with other textural types, which have higher concentrations: hematite replacing feldspar (consistent concentrations in the range 1400–2400 ppm), granoblastic hematite (400–1000 ppm), and colloform hematite (160–1200 ppm). Granoblastic hematite also displays the relatively highest concentrations of Sc and Zr among the different textural types, albeit at very low concentrations (< 5 ppm Sc, < 10 ppm Zr). Hafnium is also present at measurable concentrations.

## 7. Discussion

Hematite from OD displays a variety of textures accompanied by distinctive trace element signatures and REY-fractionation trends. As shown here, and previously (Ciobanu et al., 2013, 2015; Cook et al., 2016; Verdugo-Ihl et al., 2017), a granitophile-signature prevails throughout the hematite in the deposit irrespective of textures.

### 7.1. *Incorporation of granitophile elements in hematite*

Hematite incorporates elements in VI-coordinated positions, permitting accommodation of a wide range of foreign cations at concentrations that can attain wt% levels. Substituting cations include those with higher oxidation states as shown by X-ray absorption near-edge spectroscopy (XANES) studies for $U^{6+}$ (Duff et al., 2002) and $W^{6+}$ (Kreissl et al., 2016) in synthetic and natural hematite ($\alpha$-$Fe_2O_3$). Raman spectral evidence was also given for $W^{6+}$ in hematite from an oxidation zone in the Western Rhodopes, Bulgaria (Tarassov et al., 2002).

The presence of U(-Pb), W, Sn and Mo in the lattice of zoned hematite from OD, for which LA-ICP-MS and transmission electron microscopy (TEM) data were reported by Ciobanu et al. (2013), is here attested to by EPMA data for the first time. The necessity to consider $Me^{6+}$ (Me: U, W, Mo) in U-rich hematite from OD (up to 0.013 apfu, assuming $U^{6+}$) is based on vacancy-induced crystal-structure modifications (long-range superstructures) following the proposed substitution: $2Fe^{3+} \leftrightarrow Me^{6+} + \square$ (Ciobanu et al., 2013). A preliminary TEM study of W-rich hematite (up to 0.018 apfu) from OD shows instead a simpler, 2*a* superstructure (Liu and Ciobanu, 2016). Atomic-scale high-angular annular dark field scanning-TEM imaging of W-rich (up to 0.022 apfu) hematite which also contains a 10–20 nm-sized inclusion of ferberite ($FeWO_4$) shows defect-free, compositionally homogenous hematite, except for the presence of darker areas, a few nm in width, where the 2*a* superlattice is present suggesting O vacancies (Ciobanu et al., 2016). In this case, coherent lattice fringes imaged across the boundary between hematite and ferberite imply structural isomorphism (solid solution) between the two minerals. Considering the decrease in the oxidation state of Fe in hematite with O vacancies (Chen et al., 2008), such as the darker areas, the oxygen-deficient sites could act as catalyst for $W^{6+} \rightarrow 3Fe^{2+}$ substitution. This mechanism is different to the one suggested by EXAFS spectra showing similarities between the $W^{6+}$ and $Fe^{3+}$ position in substituted hematite (Kreissl et al., 2016).

Comparable suggestions for substitutional mechanisms involving $Fe^{2+}$ have been put forward to explain incorporation of Sn in hematite with up to 2.26 wt% $SnO_2$ (~0.024 apfu Sn) in oscillatory-zoned hematite from placer deposits in Canadian Creek, Yukon, Canada (Barkov et al., 2008). These authors discussed several substitutional mechanisms but concluded that the most likely is $Sn^{4+} + Fe^{2+} \leftrightarrow 2Fe^{3+}$, whereby co-present $Al^{3+}$ would minimise lattice strain.

In contrast to the granitophile elements discussed in the above paragraphs, very little is known about the presence of Mo in natural hematite. This can however be considered, like U or W, to have a

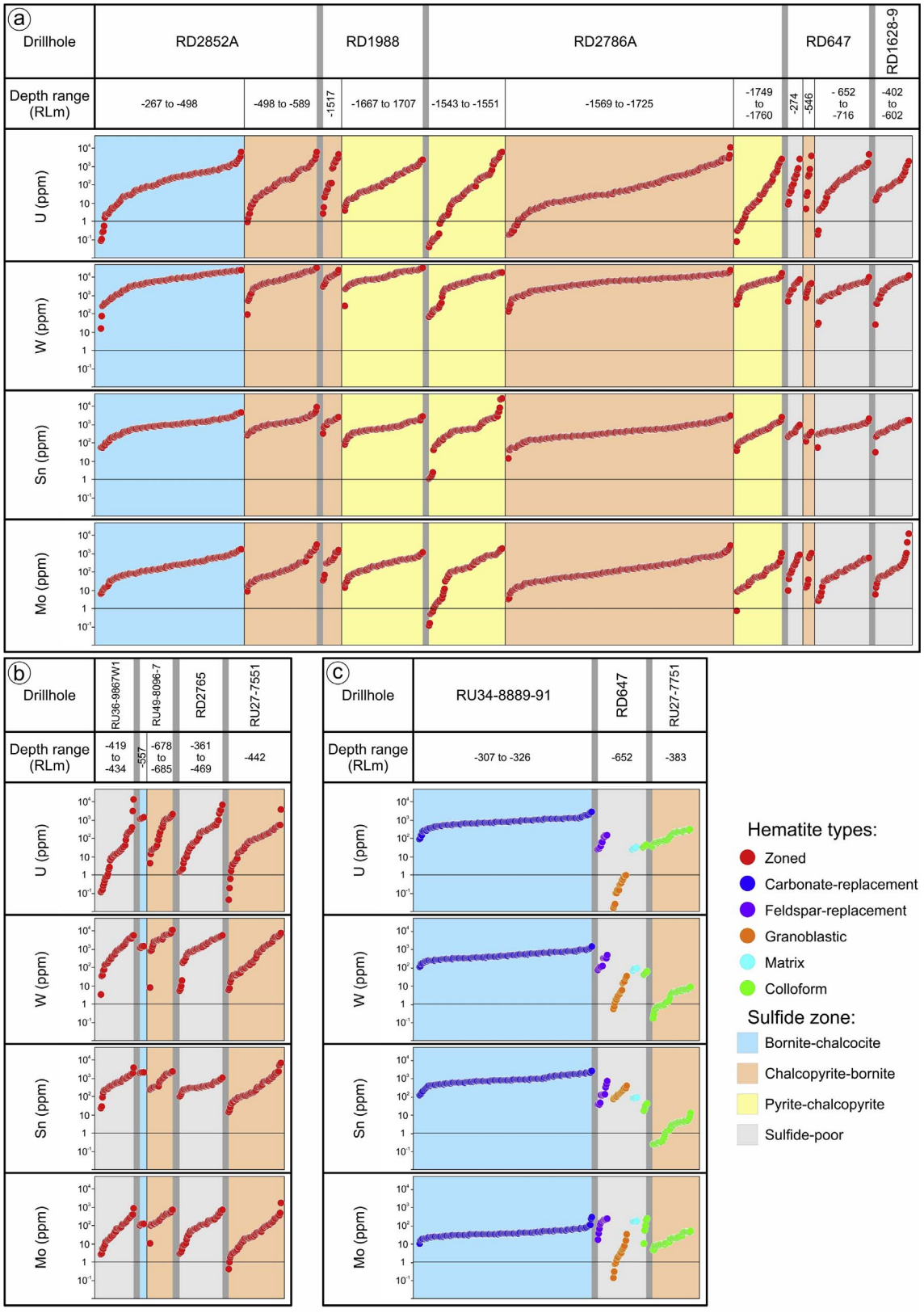


**Fig. 14.** Diagrams showing granitophile element concentrations in individual analyses arranged in ascending order by sulphide zones and textural type. (a) Zoned hematite, SE lobe. (b) Zoned hematite, deposit middle and NW arm. (c) Other textural categories in SE lobe, middle and NW arm.

hexavalent oxidation state. The assumption of a higher oxidation state for U, W and Mo in early hydrothermal fluids at OD is, however, somewhat contradictory to that made for 'primary' uraninite (Macmillan et al., 2016a). In uraninite, a change in the oxidation state from $U^{4+}$ to $U^{6+}$ was invoked to track the evolution from the earliest (primary) to latest, partially replaced, recrystallised, or newly-precipitated generations of uraninite. XANES studies are necessary on each of the two minerals to assess the oxidation states of the substituting

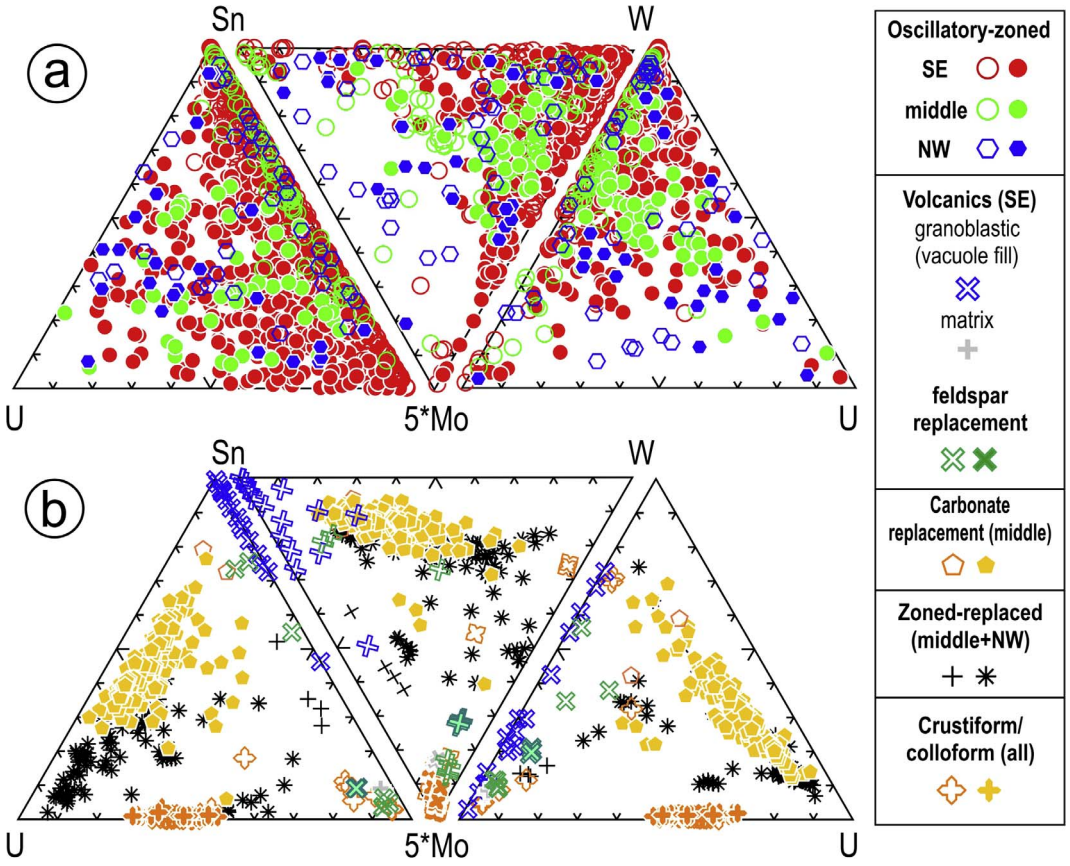


**Fig. 15.** Ternary plots of U-Sn-Mo(*5), W-Sn-Mo(*5) and U-W-Mo(*5) showing relative enrichment of granitophile elements in different textural types of hematite. (a) Granitophile-zoned hematite from the SE lobe, the deposit middle, and the NW arm. (b) Other categories from various locations. Filled symbols correspond to U-rich hematite (> 122 ppm).

elements.

### 7.2. REY and other trace element signatures in hematite – evolving fluids

Concentrations of REY within OD hematite are subordinate to those in other minerals that are better REY-carriers, e.g., uraninite (Macmillan et al., 2016a), or apatite (Krneta et al., 2017). Nonetheless, some categories of hematite contain up to tens or hundreds ppm ΣREY, e.g., zoned hematite from depth in the SE lobe, and carbonate replacement plus zoned overprinted categories. Although the measured REY concentrations likely relate not only to lattice-bound elements substituting for Fe (e.g., map in Fig. 10) but also to the presence of discrete, sub-μm-sized REE-mineral inclusions, the consistency of chondrite-normalized REY-fractionation trends (Fig. 17) suggests that REY signatures can be used as geochemical tracers for fluid evolution at OD. In hydrothermal systems, the transport and deposition of REE is controlled by the stability and availability of suitable ligands to complex REE, and the relative solubilities of REE-bearing phases. Experimental and thermodynamic calculations of REE stability, transport and deposition conclude that chloride and sulfate species dominate solution transport whereas fluoride, carbonate and phosphate are important as depositional ligands (Migdisov et al., 2016 and references therein).

The subtle variations in zoned hematite, otherwise characterized by comparable, slightly concave, relatively LREE-enriched fractionation trends, relate mostly to Eu- and Y-anomalies. The transition from a negative to a positive Eu-anomaly can be correlated with the strong effect of pH in constraining the dominant REE-(chloride) aqueous transport complexes, impacting on the relative stabilities of $Eu^{2+}$ versus $Eu^{3+}$. Fluids of variable pH from mildly acidic (sericite-stable) to alkaline (carbonate-buffered) are interpreted to explain comparable changes in Eu-anomalies recorded by apatite from early to late hydrothermal stages at OD (Krneta et al., 2017). The presence of a strong negative Y-anomaly, recorded in one-third of the analysed hematites, is suggestive of co-precipitation of relatively Y-rich phases such as xenotime or monazite.

The slightly HREE-enriched fractionation trends recorded in carbonate replacement and overprinted zoned hematite can be related either to down-T fractionation, or to depositional controls offered by HREE-fluoride stability relative to that of LREE-chloride complexes (Migdisov et al., 2016). On the other hand, highly acidic HF-rich fluids can transport $NbF_2(OH)_3$ complexes, and such acidic fluids, if they interact with carbonates, will be neutralised (Timofeev et al., 2015). This depositional mechanism can also explain the high concentrations of Nb (thousands of ppm) and other HFSE (V, Th) in carbonate replacement and overprinted zoned hematite categories.

All other categories of hematite: volcanic-hosted (except zoned hematite from the same samples, which resemble zoned hematite elsewhere) and colloform, display similar REY fractionation patterns. These feature relatively flat trends, slightly LREE-rich for volcanic-hosted categories, and slight variation in the size and sign of Eu- and/or Y-anomalies, but are distinct from those shown by zoned hematite (Fig. 17). Such trends are comparable with chondrite-normalized REY patterns for some Fe-oxides and/or hydroxides observed from BIF-supergene environments (e.g., Keyser et al., in review). The latter are interpreted to represent the signatures of low-T (< 250 °C) submarine thermal springs associated with young volcanoes (Michard et al., 1993). Comparable seafloor paleo-vents could have been associated with formation of volcanic-hosted (granoblastic, matrix and feldspar replacement) hematite considering that these rocks may well have formed in a submarine environment.

Volcanic-hosted and colloform hematites are, however, clearly distinguishable from one another in terms of the concentrations of other

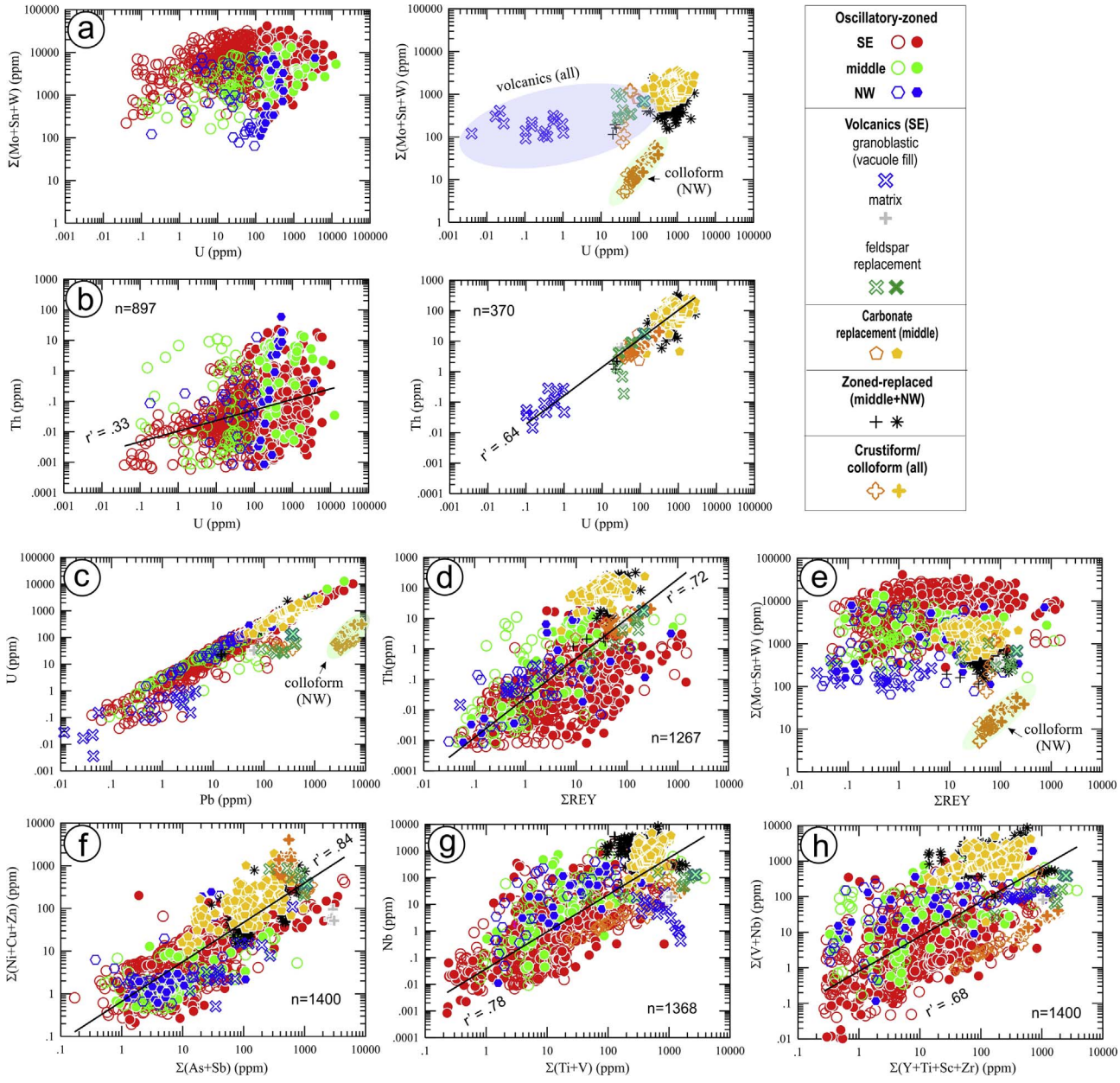


**Fig. 16.** Scatterplots for selected trace elements. (a) U *vs.* Mo + Sn + W, (b) U *vs.* Th, (c) Pb *vs.* U, (d) ΣREY *vs.* Th, (e) ΣREY *vs.* Mo + Sn + W, (f) As + Sb *vs.* Ni + Cu + Zn, (g) Ti + V *vs.* Nb, and (h) Sc + Ti + Y + Zr *vs.* V + Nb. Filled symbols correspond to U-rich hematite (> 122 ppm).

trace elements, notably their Sn-Ti-Zr-Sc and Cu-Zn-As signatures (Figs. 12 and 16). Colloform hematite from the NW arm is an outlier on most of the plots (Figs. 15b and 16), but particularly on those involving Th, U and radiogenic Pb. They may plausibly represent a much younger (post-IOCG) hematite, not least because they also strongly resemble colloform magnetite within veinlets from ~820 Ma Gairdner dikes documented from OD (Apukhtina et al., 2016).

The relatively strong correlations between different groups of elements including REY, chalcophile, transition metals and HFSE (Fig. 16f–h) in all granitophile-rich hematite categories show the complex evolution of trace element signatures across the OD deposit. Multivariate statistical analysis will be employed to better define such signatures and their potential for spatial ore vectoring.

### 7.3. Chemical oscillators and recycling trace elements during their overprint

Oscillatory zoning, in which chemical composition varies from core to rim, is a common feature of crystal growth from fluids of complex chemistry if ionic diffusion in the solid is much slower than that in the fluid. Such processes have been reproduced experimentally using major-element variation in solid-solution series (e.g., $(Ba,Sr)SO_4$; Putnis et al., 1992). Chemical-oscillatory growth can be controlled by either extrinsic (external) or intrinsic (internal) factors. Macroscopic and cellular automata models have simulated experimentally-produced patterns in $(Ba,Sr)SO_4$ without an external template, proving that spontaneous spatiotemporal patterns can be generated by non-linear systems driven away from thermodynamic equilibrium (L'Heureux and Katsev, 2006). Of direct relevance here is that, in such models, small fluctuations in element concentrations within aqueous solution may contribute to the development of oscillatory zoning by causing noise-induced transitions in the crystal growth, thus explaining both the textural variety and differences in the relative concentrations of the granitophile elements measured or mapped in zoned hematite (Figs. 3, 6, 8–11 and 15a). Such incredible variation, sometimes observed between grains in the same sample, as well as the lack of obvious, reproducible trends throughout the deposit, may be indicative of

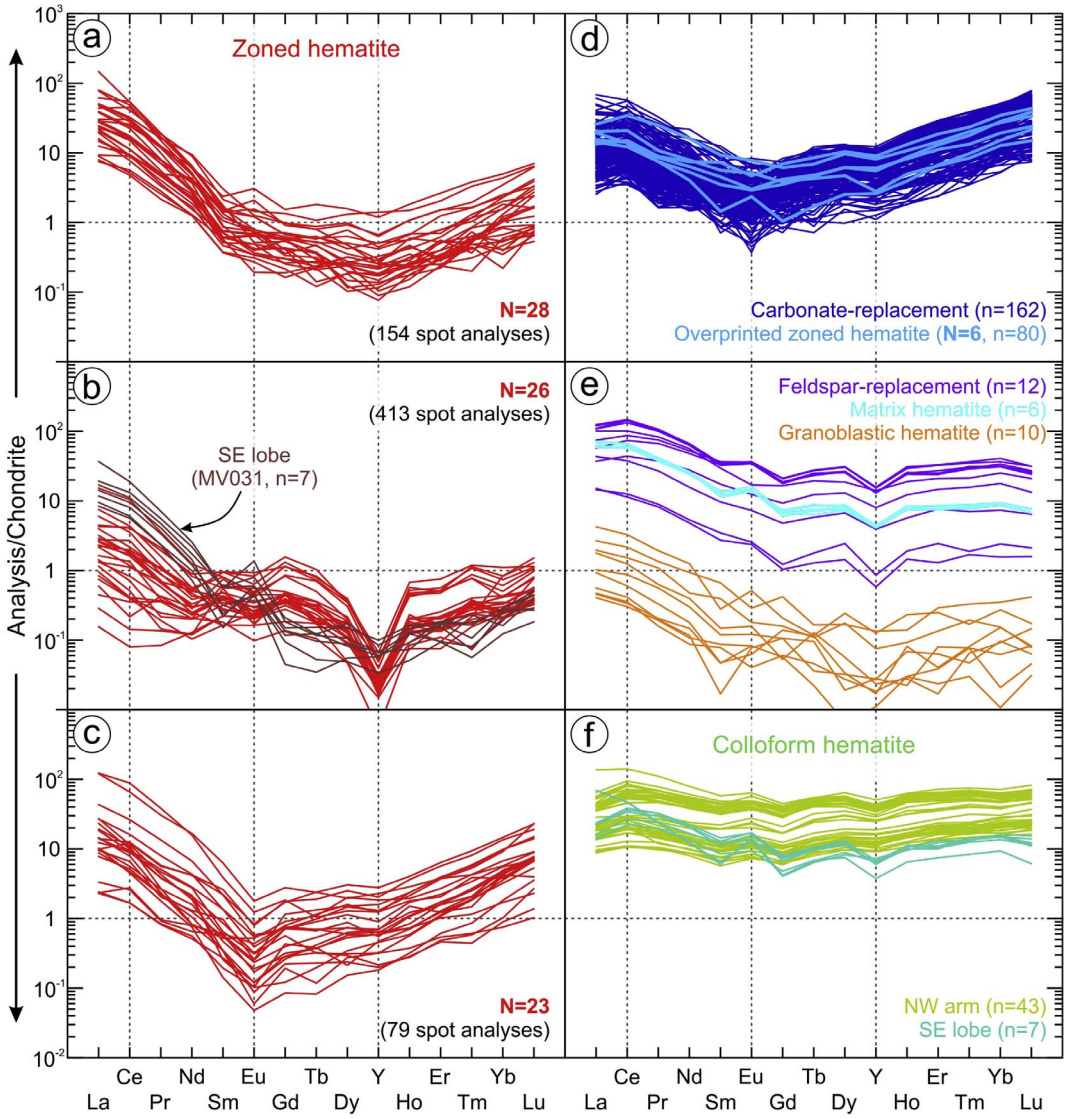


**Fig. 17.** Chondrite-normalized REY-fractionation trends for granitophile-rich hematite categories as marked. The trends depicted for zoned hematite (a-c) are not specific to any location or lithology in the deposit. N = sample averages (geometric mean); n = number of spot analyses. See text for additional explanation.

self-organising phenomena whereby small rather than systematic compositional variation within the same fluids induces chemical oscillations during hematite growth. The REY-fractionation trends for zoned hematite, which typically lack systematic trends within an individual sample, from one sample to another, or throughout the deposit, also support this idea.

Textural characterization and element mapping of zoned hematite shows several key aspects instructive for understanding overprinting in terms of cation exchange, nucleation of inclusions, partial replacement and recrystallisation (Fig. 18). Whereas, the zoned hematite generally displays variations on the theme of pseudomorphic replacement that are generically attributable to reactions that couple dissolution with reprecipitation reactions (CDRR; Putnis, 2002), there are two major lines of fluid-hematite interaction shown schematically in Fig. 18.

The first type (1), also discussed in previous studies (Ciobanu et al., 2013; Cook et al., 2016), is characterized by corrosive replacement boundaries presumably produced by acidic, HF-rich (?) fluids leading to intense porosity, obliteration of zoning, and strong depletion of trace elements, particularly the granitophile elements (case 1a). A range of minute mineral inclusions formed from the removed trace elements can be trapped within the pores. These inclusions display a continuous range of textures, and vary in density, from scattered to dense swarms, even within grains from the same sample. CDRR reactions are promoted by transient porosity and depending upon the rates of reaction, some pores remain open whereas others are rapidly closed and obliterated (Putnis, 2015). Such inclusions may provide the ingredients for a second generation of granitophile-rich hematite, the overprinted zoned type, should the grain undergo re-crystallisation (case 1b). The most compelling case is represented by the observation of REE-fluorocarbonates within the recrystallised patterns (Fig. 7b). This is also further support for the presumption of F-rich fluids (case 1c).

The second type (2) is, however, new and shows fluids at disequilibrium only with respect to certain elements, leading to selective removal of, for example, W but not Sn (case 2a). The textures can be considered to evolve via sharp interface boundaries since zonation patterns are well preserved. The same can be invoked to explain recycling of granitophile elements, e.g., Mo, into subsequent cycles of zoning with chalcophile elements, e.g., Cu, As, Sb (case 2b), typifying hematite from sulphide-poor intervals.

Such selective removal of trace elements can be suggested by redox changes in the fluid, affecting elements with differences in the stability of cationic oxidation states ($Sn^{4+}$ versus $W^{6+}$). Reducing fluids can be associated with sulphide-depleted intervals featuring barite veining, in which native copper and Cu-Au alloys are also stable (Ciobanu, 2015).

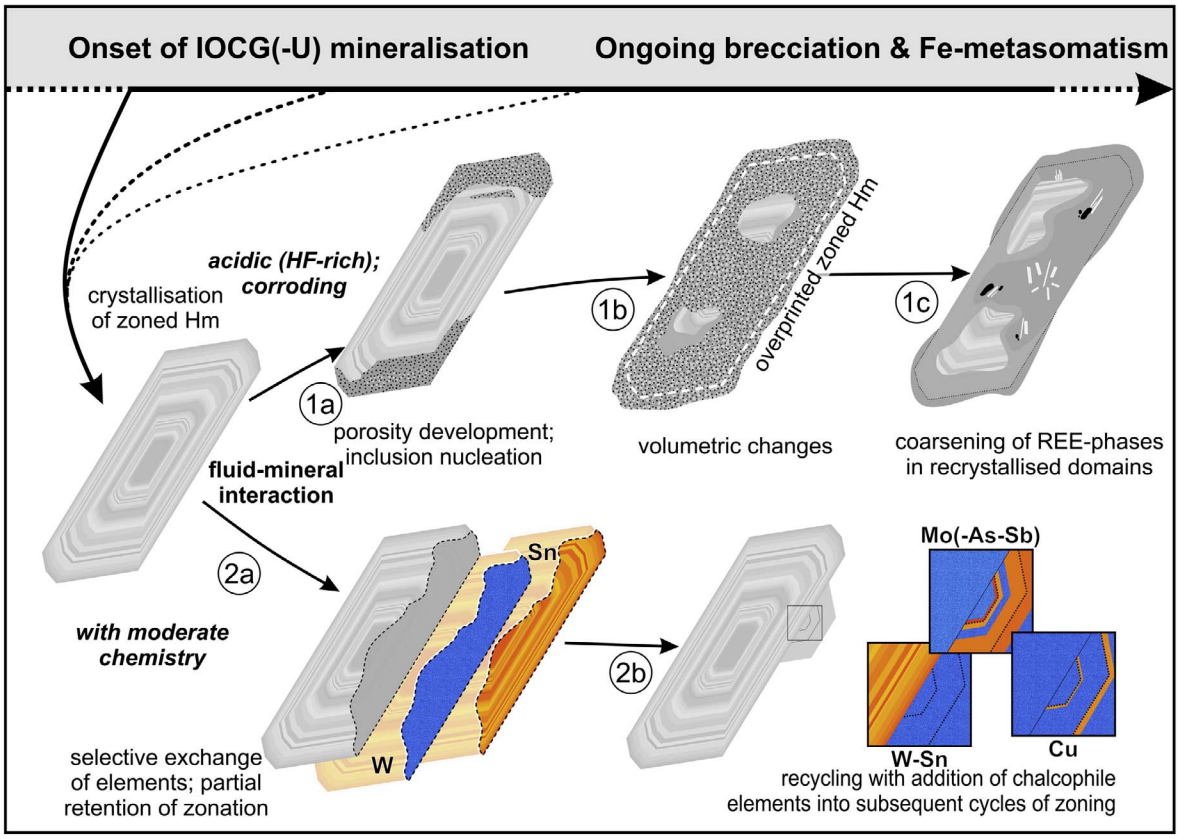


**Fig. 18.** Schematic showing the main types of zoned hematite overprint preserving granitophile-rich signatures. Textures and trace element signatures are interpreted to result from coupled dissolution reprecipitation reactions but with various scenarios for the fluids as marked. See text for additional explanation.

Case 2a is just ~200 m away from 2b.

Both types of interaction preserve, albeit in different ways, the initial granitophile signatures of zoned hematite either in new, recrystallised grains, or as discrete mineral inclusions. At OD, comparable selective trace element removal has been shown for uraninite during strain-induced radiogenic decay of U (Macmillan et al., 2016b), as well as CDRR-driven replacement of uraninite by Cu-Fe-sulphides (Macmillan et al., 2016c). The hypotheses discussed above will be constrained in the future by nanoscale studies of hematite addressing the relative orientation of the hematite across replacement boundaries.

### *7.4. Hematite from the Olympic Dam orebody – defining the archetype for IOCG deposits*

Taken together, the complexity of trace element signatures as defined here, particularly the links between the U-W-Sn-Mo signatures with REY, HFSE and chalcophile elements (Cu, Zn, As, Sb) in hematite, the major component of the deposit, represents a proof-of-concept for the conceptual framework of IOCG system genesis, which predicts enrichment in such elements (Groves et al., 2010 and references therein). In such models, metal sources are tied to magmas originating from metasomatised subcontinental lithospheric mantle with transfer of volatiles and metals between (volatile-rich) alkaline basic and ultrabasic magmas, and felsic melts formed in the lower crust. Such melts are the source for bimodal magmatism in the upper crust as proven at OD (Huang et al., 2015) and elsewhere in the Olympic Cu-Au Province (e.g., at Hillside; Conor et al., 2010).

The maar setting assigned to OD in such schematics is, however, incompatible with recent studies that have addressed and reconstructed sedimentary successions observed at upper levels of the deposit (McPhie et al., 2016), or the proposed depth of granite emplacement (Kontonikas-Charos et al., 2017a). In addition, the obliteration of transient porosity developed during CDR reactions confines metals and allows for preservation of geochemical signatures as discussed here for hematite and elsewhere for feldspars and uraninite (Kontonikas-Charos et al., 2017a,b; Macmillan et al., 2016a,b,c). Such evidence, as well as the preservation of high-T, primary Cu-(Fe)-sulphides throughout the vertical zonation (Ciobanu et al., 2017), suggest that Cu-U mineralisation formed at depth, prior to RDG uplift.

Recent LA-ICP-MS U-Pb dating of zoned hematite using the same sample suite across OD (Courtney-Davies et al., 2017) has shown two distinct hematite age groups. The oldest group, including some of the published ages for the high-grade ore (Ciobanu et al., 2013; Courtney-Davies et al., 2016) and spanning the vertical sulphide-zonation in the SE lobe (confirmed by high-precision ID-TIMS U-Pb dating; Courtney-Davies et al., 2017) closely resembles U-Pb zircon ages for the RDG (1593.9 ± 0.5 Ma; Jagodzinski, 2014), thus clearly relating mineralisation to emplacement of the host granite. Based on the consistency of the oldest hematite ages and the prominent enrichment of U, W Sn and Mo in hematite, a granitic source for the hydrothermal fluids is inferred. Ongoing high-precision dating of zoned hematite from volcanoclastic rocks and sedimentary rocks will provide a time-space framework for the deposit evolution.

Olympic Dam was one deposit considered to define IOCG mineralisation as a distinct style (Hitzman et al., 1992) but ongoing work highlights the ingredients necessary to refine broader IOCG models. The U-W-Sn-Mo signature, retained throughout the different textural types of hematite described here, can be considered one of the defining characteristics of such an archetype. Despite its simple chemistry, the crystal-structural modularity of hematite can adapt and retain evolving fluid signatures so long as the main type of fluid-rock interaction is via coupling dissolution with re-precipitation rates.

## 8. Outlook and implications

The widespread presence of hematite enriched in granitophile elements is hitherto unreported from other locations, although enrichment in individual elements is well-documented in the literature. For example, maximum concentrations of up to 4.96 wt% $WO_3$ (~0.034 apfu W), accompanied by 0.13 wt% $SnO_2$ (~0.001 apfu Sn), are documented from epithermal veins with exotic Cu-Bi-sulphosalts (Banska Stiavnica, Slovak Republic; Sejkora et al., 2015). Simultaneous enrichment of both W and Sn in hematite, whether as discrete mineral inclusions or lattice-bound substitution, thus appears to be relatively common, even if a simultaneous enrichment in U and Mo is less commonly reported. Nonetheless, hematite from other IOCG systems in the Olympic Cu-Au Province, South Australia, and also from the Carajás Province, Brazil, possess trace-element signatures that resemble those observed at OD (Courtney-Davies et al., 2016). Comparable W ± Sn-enriched signatures were recently recognised in the skarn-like overprint of BIF-mineralisation from the Island Dam prospect (located ~17 km SE from the OD deposit; Keyser et al., 2017), further emphasizing that enrichment in granitophile elements is a common feature of Fe-oxides across the Olympic Cu-Au Province. In IOCG systems with skarn alteration, however, garnets from the granite series preferentially partition comparable concentrations of granitophile elements instead of Fe-oxides (e.g., Hillside deposit, Yorke Peninsula; Ismail et al., 2014). An association of U with Fe-oxides appears widespread (e.g., Karkhanavala, 1958; Wernicke and Lippolt, 1993), yet wt% levels, such as those reported by Ciobanu et al. (2013), or in this study have not been published for hematite from hydrothermal deposits elsewhere.

CDR-reactions are recognised as driving element exchange during hydrothermal alteration in IOCG-systems and, as shown here, are important for partially preserving the granitophile signatures throughout various hematite categories. CDRR are invoked as a fundamental requisite for formation of IOCG-systems, whereby sodic alteration (albitization) contributes towards the total available REE budget (Kontonikas-Charos et al., 2014, 2018). Indeed, such reactions are shown to be widespread at OD across disparate mineral groups (e.g., Macmillan et al., 2016a,b, Kontonikas-Charos et al., 2017b). As noted by Ciobanu et al. (2017), CDRR may be characteristic for, and inherent to, formation of giant, high-grade deposits of this type.

As seen from OD, Fe-oxides are among the minerals that have been repeatedly formed, reworked and overprinted by subsequent cycles of brecciation, fluid-mineral reaction, remobilization and recrystallisation within the same sample (Ciobanu et al., 2013; Cook et al., 2016), and throughout the orebody as shown here. Despite this, aspects of the primary geochemical signatures survive these processes and can therefore be traced.

Lastly, the presence of granitophile elements in hematite carries relevance for definition of a hypothetical future resource. Locally, concentrations of W and Sn in hematite correlate with total Fe content from whole-rock assay data, indicating increase with the degree of Fe-metasomatism (Fig. 2d, e). Hematite is already recognised as the 4th most important U-bearing phase at OD after uraninite, coffinite and brannerite (Ehrig et al., 2012), and is probably by far the most important W-, Sn- and Mo-bearing phase in the deposit by mass.

## Acknowledgements

This work is a contribution to the 'FOX' project (Trace elements in iron oxides: deportment, distribution and application in ore genesis, geochronology, exploration and mineral processing), supported by BHP Olympic Dam and the South Australian Government Mining and Petroleum Services Centre of Excellence. We extend thanks to staff at Adelaide Microscopy, particularly Benjamin Wade, for assistance with microanalysis. Last but not least, we acknowledge valuable comments from reviewers Ian Graham and Alexandre Cabral and *Ore Geology Reviews* Chief Editor Franco Pirajno, which helped us improve expression of our results and interpretations.

## Appendix A. Supplementary data

Supplementary data associated with this article can be found, in the online version, at http://dx.doi.org/10.1016/j.oregeorev.2017.10.007.

## References

Apukhtina, O.B., Kamenetsky, V.S., Ehrig, K., Kamenetsky, M.B., McPhie, J., Maas, R., Meffre, S., Goermann, K., Rodermann, T., Cook, N.J., Ciobanu, C.L., 2016. Postmagmatic magnetite–apatite assemblage in mafic intrusions: a case study of dolerite at Olympic Dam, South Australia. Contrib. Mineral. Petrol. 171. https://http://dx.doi.org/10.1007/s00410-015-1215-7.

Barkov, A.Y., Martin, R.F., Shi, L., LeBarge, W., Fedortchouk, Y., 2008. Oscillatory zoning in stanniferous hematite and associated W- and Bi-rich minerals from Canadian Creek, Yukon, Canada. Can. Mineral. 46, 59–72. http://dx.doi.org/10.3749/canmin.46.1.59.

BHP Billiton, 2016. Annual Report 2016. http://www.bhpbilliton.com/~/media/bhp/documents/investors/annual-reports/2016/bhpbillitonannualreport2016.pdf?la=en.

Broughm, S.G., Hanchar, J.M., Tornos, F., Westhues, A., Attersley, S., 2017. Mineral chemistry of magnetite from magnetite-apatite mineralization and their host rocks: examples from Kiruna, Sweden, and El Laco, Chile. Miner. Deposita (in press). https://doi.org/10.1007/s00126-017-0718-8.

Chen, Z., Cvelbar, U., Mozetič, M., He, J., Sunkara, M.K., 2008. Long-range ordering of oxygen-vacancy planes in α-$Fe_2O_3$ nanowires and nanobelts. Chem. Mater. 20 (9), 3224–3228. http://dx.doi.org/10.1021/cm800288y.

Ciobanu, C.L., 2015. Trace element signatures in sulphides at Olympic Dam and satellite prospects. Unpublished report for BHP Billiton Olympic Dam, 260 pp.

Ciobanu, C.L., Wade, B.P., Cook, N.J., Schmidt Mumm, A., Giles, D., 2013. Uranium-bearing hematite from the Olympic Dam Cu–U–Au deposit, South Australia: a geochemical tracer and reconnaissance Pb–Pb geochronometer. Precambr. Res. 238, 129–147. http://dx.doi.org/10.1016/j.precamres.2013. 10.007.

Ciobanu, C.L., Cook, N.J., Ehrig, K., Wade, B.P., Kamenetsky, V.S., 2015. Trace element signatures in iron oxides from the Olympic Dam IOCG deposit, South Australia. 13th SGA Biennial Meeting 2015. Miner. Resour. Sustainable World 3, 1071–1074.

Ciobanu, C.L., Cook, N.J., Ehrig, K., Courtney-Davies, L., Keyser, W., Wade, B.P., Maunders, C., Kamenetsky, V.S., 2016. Towards a suitable natural standard for routine U-Pb dating of iron oxides. Abstract, Australian Earth Sciences Convention, Adelaide.

Ciobanu, C.L., Cook, N.J., Ehrig, K., 2017. Ore minerals down to the nanoscale: Cu-(Fe)-sulphides from the iron oxide copper gold deposit at Olympic Dam, South Australia. Ore Geol. Rev. 81, 1218–1235. http://dx.doi.org/10.1016/j.oregeorev.2016.08.015.

Conor, C., Raymond, O., Baker, T., Teale, G., Say, P., Lowe, G., 2010. Alteration and mineralisation in the Moonta-Wallaroo Cu–Au mining field region, Olympic Domain, South Australia. In: In: Porter, T.M. (Ed.), Hydrothermal Iron Oxide Copper-Gold and Related Deposits, vol. 3. PGC Publishing, Adelaide, pp. 1–24.

Cook, N.J., Ciobanu, C.L., George, L., Zhu, Z.-Y., Wade, B., Ehrig, K., 2016. Trace element analysis of minerals in magmatic-hydrothermal ores by laser ablation inductively-coupled plasma mass spectrometry: approaches and opportunities. Minerals 6 (4), 111. http://dx.doi.org/10.3390/min6040111.

Courtney-Davies, L., Zhu, Z., Ciobanu, C.L., Wade, B.P., Cook, N.J., Ehrig, K., Cabral, A.R., Kennedy, A., 2016. Matrix-matched iron-oxide laser Ablation ICP-MS U-Pb geochronology using mixed solution standards. Minerals 6 (3), 85. http://dx.doi.org/10.3390/min6030085.

Courtney-Davies, L., Ciobanu, C.L., Cook, N.J., Verdugo-Ihl, M., Tapster, S.R., Condon, D. J., Kennedy, A.K., Ehrig, K., Wade, B/P., Gilbert, S.E. 2017. Oscillatory-zoned hematite: a reliable U-Pb mineral geochronometer. Abstract, Goldschmidt 2017, Paris, France, August 13–18.

Creaser, R.A., 1989. The Geology and Petrology of Middle Proterozoic felsic Magmatism of the Stuart Shelf, South Australia. Unpublished PhD thesis, La Trobe University.

Dare, S.A.S., Barnes, S.-J., Beaudoin, G., 2015. Did the massive magnetite "lava flows" of El Laco (Chile) form by magmatic or hydrothermal processes? New constraints from magnetite composition by LA-ICP-MS. Miner. Deposita 50, 607–617. http://dx.doi.org/10.1007/s00126-014-0560-1.

Duff, M.C., Coughlin, J.U., Hunter, D.B., 2002. Uranium co-precipitation with iron oxide minerals. Geochim. Cosmochim. Acta 66, 3533–3547. http://dx.doi.org/10.1016/S0016-7037(02)00953-5.

Ehrig, K., McPhie, J., Kamenetsky, V., 2012. Geology and Mineralogical Zonation of the Olympic Dam Iron Oxide Cu-U-Au-Ag Deposit, South Australia. In J.W. Hedenquist, M. Harris, F. Camus (Eds.), Geology and Genesis of Major Copper Deposits and Districts of the World: A Tribute to Richard H. Sillitoe, Society of Economic Geologists, Special Publication 16, pp. 237–267.

Fanning, C.M., Flint, R.B., Parker, A.J., Ludwig, K.R., Blissett, A.H., 1988. Refined Proterozoic evolution of the Gawler Craton, South Australia, through U-Pb zircon geochronology. Precambr. Res. 40–41, 363–386. http://dx.doi.org/10.1016/0301-9268(88)90076-9.

Groves, D.I., Bierlein, F.P., Meinert, L.D., Hitzman, M.W., 2010. Iron Oxide Copper-Gold (IOCG) deposits through earth history: implications for origin, lithospheric setting, and distinction from other epigenetic iron oxide deposits. Econ. Geol. 105, 641–654. http://dx.doi.org/10.2113/gsecongeo.105.3.641.

Hitzman, M.W., Oreskes, N., Einaudi, M.T., 1992. Geological characteristics and tectonic

setting of Proterozoic iron oxide (Cu-U-Au-REE) deposits. Precambr. Res. 58, 241–287. http://dx.doi.org/10.1016/0301-9268(92)90121-4.

Huang, Q., Kamenetsky, V.S., McPhie, J., Ehrig, K., Meffre, S., Maas, R., Thompson, J., Kamenetsky, M., Chambefort, I., Apukhtina, O., Hu, Y., 2015. Neoproterozoic (ca. 820–830 Ma) mafic dykes at Olympic Dam, South Australia: links with the Gairdner Large Igneous Province. Precambr. Res. 271, 160–172. http://dx.doi.org/10.1016/j.precamres.2015.10.001.

Huang, Q., Kamenetsky, V.S., Ehrig, K., McPhie, J., Kamenetsky, M., Cross, K., Meffre, S., Agangi, A., Chambefort, I., Direen, N.G., Maas, R., Apukhtina, O., 2016. Olivine-phyric basalt in the Mesoproterozoic Gawler silicic large igneous province, South Australia: examples at the Olympic Dam Iron Oxide Cu–U–Au–Ag deposit and other localities. Precambr. Res. 281, 185–199. http://dx.doi.org/10.1016/j.precamres.2016.05.019.

Ismail, R., Ciobanu, C.L., Cook, N.J., Teale, G.S., Giles, D., Schmidt Mumm, A.S., Wade, B., 2014. Rare earths and other trace elements in minerals from skarn assemblages, Hillside iron oxide–copper–gold deposit, Yorke Peninsula, South Australia. Lithos 184–187, 456–477. http://dx.doi.org/10.1016/j.lithos. 2013.07.023.

Jagodzinski, E.A., 2005. Compilation of SHRIMP U-Pb geochronological data Olympic Domain, Gawler Craton, South Australia. Geoscience Australia Record 2005/20.

Jagodzinski, E.A., 2014. The Age of Magmatic and Hydrothermal Zircon at Olympic Dam. In: Proceedings of 2014 Australian Earth Sciences Convention (AESC), Sustainable Australia, Newcastle, NSW, Australia, 7–10 July 2014; vol. 110, p. 260.

Karkhanavala, M.D., 1958. On radioactive uraniferous iron oxides. Geochim. Cosmochim. Acta 15, 229–236. http://dx.doi.org/10.1016/0016-7037(58)90060-7.

Keyser, W.M., Ciobanu C.L., Cook, N.J., Courtney-Davies L., Ehrig K., Gilbert S., McPhie, J., 2017. Links between sedimentary protoliths and IOCG-skarn alteration, Island Dam, South Australia, Extended abstract, 14th Biennial SGA Conference, Québec, Canada, vol. 3, pp. 935-938.

Keyser, W., Ciobanu, C.L., Cook, N.J., Johnson, G., Feltus, H., Johnson, S., Dmitrijeva, M., Ehrig, K., Nguyen, P.T. (in review) Petrography and trace element signatures of iron-oxides in deposits from the Middleback Ranges, South Australia: from banded iron formation to ore. Ore Geol. Rev.

Knipping, J.L., Bilenker, L.D., Simon, A.C., Reich, M., Barra, F., Deditius, A.P., Lundstrom, C., Bindeman, I., Munizaga, R., 2015a. Giant Kiruna-type deposits form by efficient flotation of magmatic magnetite suspensions. Geology 43, 591–594. http://dx.doi.org/10.1130/G36650.1.

Knipping, J.L., Bilenker, L.D., Simon, A.C., Reich, M., Barra, F., Deditius, A.P., Wälle, M., Heinrich, C.A., Holtz, F., Munizaga, R., 2015b. Trace elements in magnetite from massive iron oxide-apatite deposits indicate a combined formation by igneous and magmatic-hydrothermal processes. Geochim. Cosmochim. Acta 171, 15–38. http://dx.doi.org/10.1016/j.gca. 2015.08.010.

Kontonikas-Charos, A., Ciobanu, C.L., Cook, N.J., 2014. Albitization and redistribution of REE and Y in IOCG systems: Insights from Moonta-Wallaroo, Yorke Peninsula, South Australia. Lithos 208–209, 178–201. http://dx.doi.org/10.1016/j.lithos.2014.09.001.

Kontonikas-Charos, A., Ciobanu, C.L., Cook, N.J., Ehrig, K., Krneta, S., Kamenetsky, V.S., 2017a. Feldspar evolution in the Roxby Downs Granite, host to Fe-oxide Cu-Au-(U) mineralisation at Olympic Dam, South Australia. Ore Geol. Rev. 80, 838–859. http://dx.doi.org/10.1016/j.oregeorev.2016.08.019.

Kontonikas-Charos, A., Ciobanu, C.L., Cook, N.J., Ehrig, K., Ismail, R., Krneta, S., Basak, A., 2017b. Feldspar mineralogy and rare earth element (re)mobilization in iron-oxide copper gold systems from South Australia: a nanoscale study. Mineral. Mag. http://dx.doi.org/10.1180/minmag.2017. 081.040.

Kontonikas-Charos, A., Ciobanu, C.L., Cook, N.J., Ehrig, K., Krneta, S., Kamenetsky, V.S., 2018. Rare earth element geochemistry of feldspars: examples from Fe-oxide Cu-Au systems in the olympic Cu-Au Province, South Australia. Mineral. Petrol. http://dx.doi.org/10.1007/s00710-017-0533-z. in press.

Kreissl, S., Bolanz, R., Göttlicher, J., Steininger, R., Tarassov, M., Markl, G., 2016. Structural incorporation of $W^{6+}$ into hematite and goethite: a combined study of natural and synthetic iron oxides developed from precursor ferrihydrite and the preservation of ancient fluid compositions in hematite. Am. Mineral. 101, 2701–2715. http://dx.doi.org/10.2138/am-2016-5690.

Krneta, S., Ciobanu, C.L., Cook, N.J., Ehrig, K., Kontonikas-Charos, A., 2017. Rare earth element behaviour in apatite from the Olympic Dam Cu–U–Au–Ag deposit, South Australia. Minerals 7 (8), 135. https://http://dx.doi.org/10.3390/min7080135.

L'Heureux, I., Katsev, S., 2006. Oscillatory zoning in a (Ba, Sr)SO4 solid solution: macroscopic and cellular automata models. Chem. Geol. 225 (3), 230–243. http://dx.doi.org/10.1016/j.chemgeo.2005.08.017.

Liu, Y., Ciobanu, C.L., 2016. Crystal-Structural and Nanoscale Characterization of Iron Oxides From the Olympic Dam Cu-U-Au-Ag Deposit. Unpublished Research Report. The University of Adelaide, South Australia.

Macmillan, E., Ciobanu, C.L., Ehrig, K., Cook, N.J., Pring, A., 2016a. Chemical zoning and lattice distortion in uraninite from Olympic Dam, South Australia. Am. Mineral. 101, 2351–2354. http://dx.doi.org/10.2138/am-2016-5753.

Macmillan, E., Cook, N.J., Ehrig, K., Ciobanu, C.L., Pring, A., 2016b. Uraninite from the Olympic Dam IOCG-U-Ag deposit: linking textural and compositional variation to temporal evolution. Am. Mineral. 101, 1295–1320. http://dx.doi.org/10.2138/am-2016-5411.

Macmillan, E., Ciobanu, C.L., Ehrig, K., Cook, N.J., Pring, A., 2016c. Replacement of uraninite by bornite via coupled dissolution-reprecipitation: evidence from texture and microstructure. Can. Mineral. 54, 1369–1383. http://dx.doi.org/10.3749/canmin.1600031.

McPhie, J., Kamenetsky, V.S., Chambefort, I., Ehrig, K., Green, N., 2011. Origin of the supergiant Olympic Dam Cu-U-Au-Ag deposit, South Australia: Was a sedimentary basin involved? Geology 39, 795–798. http://dx.doi.org/10.1130/G31952.1.

McPhie, J., Orth, K., Kamenetsky, V., Kamenetsky, M., Ehrig, K., 2016. Characteristics, origin and significance of Mesoproterozoic bedded clastic facies at the Olympic Dam Cu–U–Au–Ag deposit, South Australia. Precambr. Res. 276, 85–100. http://dx.doi.org/10.1016/j.precamres.2016.01.029.

Michard, A., Michard, G., Stüben, D., Stoffers, P., Cheminée, J., Binard, N., 1993. Submarine thermal springs associated with young volcanos: the Teahitia vents, Society Islands, Pacific Ocean. Geochim. Cosmochim. Acta 57, 4977–4986. http://dx.doi.org/10.1016/S0016-7037(05)80003-1.

Migdisov, A., Williams-Jones, A.E., Brugger, J., Caporuscio, F.A., 2016. Hydrothermal transport, deposition, and fractionation of the REE: Experimental data and thermodynamic calculations. Chem. Geol. 439, 13–42. http://dx.doi.org/10.1016/j.chemgeo.2016.06.005.

Putnis, A., 2002. Mineral replacement reactions: from macroscopic observations to microscopic mechanisms. Mineral. Mag. 66, 689–708. http://dx.doi.org/10.1180/0026461026650056.

Putnis, A., 2015. Transient porosity resulting from fluid-mineral interaction and its consequences. Rev. Mineral. Geochem. 80, 1–23. http://dx.doi.org/10.2138/rmg.2015.80.01.

Putnis, A., Fernandez-Diaz, L., Prieto, M., 1992. Experimentally produced oscillatory zoning in the (Ba, Sr)SO4 solid solution. Nature 358, 743–745. https://doi.org/http://dx.doi.org/10.1038/358743a0.

Reeve, J.S., Cross, K.C., Smith, R.N., Oreskes, N., 1990. Olympic Dam Copper-Uranium-gold-silver Deposit. In: F.E. Hughes (Ed.), Geology of the Mineral Deposits of Australia and Papua New Guinea, Australasian Institute of Mining and Metallurgy, pp. 1009–1035.

Sejkora, J., Števko, M., Ozdín, D., Pršek, J., Jeleň, S., 2015. Unusual morphological forms of hodrušite from the Rozália vein, Hodruša-Hámre near Banská Štiavnica (Slovak Republic). J. Geosci. 60, 11–22. http://dx.doi.org/10.3190/jgeosci.188.

Tarassov, M., Mihailova, B., Tarasova, E., Konstantinov, L., 2002. Chemical composition and vibrational spectra of tungsten-bearing goethite and hematite from Western Rhodopes, Bulgaria. Eur. J. Mineral. 14, 977–986. http://dx.doi.org/10.1127/0935-1221/2002/0014-097.

Timofeev, A., Migdisov, A.A., Williams-Jones, A.E., 2015. An experimental study of the solubility and speciation of niobium in fluoride-bearing aqueous solutions at elevated temperature. Geochim. Cosmochim. Acta 158, 103–111. http://dx.doi.org/10.1016/j.gca.2015.02.015.

van Achterbergh, E., Ryan, C.G., Jackson, S.E., Griffin, W.L., 2001. Data reduction software for LA-ICP-MS. In: P.J. Sylvester (Ed.), Laser-ablation-ICPMS in the Earth Sciences: Principles and Applications. Mineralogical Association of Canada, Short Course Series Ottawa, Ontario, Canada, vol. 29, pp. 239–243.

Verdugo-Ihl, M.R., Ciobanu, C.L., Cook., N.J., Courtney-Davies, L., Ehrig, K.J., Gilbert, S., 2017. Trace element signatures in U-W-Sn-Mo zoned hematite from the IOCG deposit at Olympic Dam, South Australia, Extended abstract, 14th Biennial SGA Conference, Québec, Canada, vol. 3, pp. 967-970.

Wernicke, R.S., Lippolt, H.J., 1993. Botryoidal hematite from the Schwarzwald (Germany): heterogeneous uranium distributions and their bearing on the helium dating method. Earth Planet. Sci. Lett. 114, 287–300. http://dx.doi.org/10.1016/0012-821X(93)90031-4.

Woodhead, J.D., Hellstrom, J., Hergt, J.M., Greig, A., Maas, R., 2007. Isotopic and elemental imaging of geological materials by laser ablation inductively coupled plasma-mass spectrometry. Geostand. Geoanal. Res. 31, 331–343. http://dx.doi.org/10.1111/j.1751-908X.2007.00104.x.

Xu, J., Ciobanu, C.L., Cook, N.J., Zheng, Y., Sun, X., Wade, B.P., 2016. Skarn formation and trace elements in garnet and associated minerals from Zhibula copper deposit, Gangdese Belt, southern Tibet. Lithos 262, 213–231. http://dx.doi.org/10.1016/j.lithos.2016.07.010.